Rankine-vortex model based assessment of CFD methods for simulating the effect of gas entrainment observed in the hot-pool of sodium coold fast breeder reactors

H. Bhatia, U. Bieder, D. Guenadou

Version of Record: https://www.sciencedirect.com/science/article/pii/S014919702100161X
Manuscript_9d1cf281144cff31ae1db4eee843e6cf

RANKINE-VORTEX MODEL BASED ASSESSMENT OF CFD METHODS FOR SIMULATING THE EFFECT OF GAS ENTRAINMENT OBSERVED IN THE HOT-POOL OF SODIUM COOLD FAST BREEDER REACTORS

H. Bhatia[1], U. Bieder[1] and D. Guenadou[2]

[1]DES-STMF, CEA, Université Paris-Saclay F-91191 Gif-sur-Yvette, France
[2]CEA Cadarache, DTN/STCP/LHC, F-13108 Saint Paul lez Durance, France

Abstract: The flow behavior in the hot pool of a compact Sodium Cooled Fast Breeder Reactor (SFR) is investigated in the MICAS facility of the CEA. Computational Fluid Dynamics (CFD) is used to assist the interpretation of the experiments by multi-scale calculations. Special attention is given to the risk of gas entrainment into the reactor core due to the formation of drain-type vortexes at the intermediate heat exchanger intakes. After theoretical considerations based on the Rankine-vortex model, the single effect gas entrainment experiment of Monji is analyzed by different CFD methods. The well-known incapacity of linear RANS models to simulate swirling flow is emphasized and limitations regarding the representation of gas cores by single-phase models are discussed. Then, the flow in the MICAS facility is analyzed by CFD using RANS and LES. The quantitative comparison between experiment and calculation shows that RANS can simulate correctly the global flow patterns in the hot pool. Small-scale drain-type vortexes have not been observed in the RANS calculations. LES can predict the onset of the formation of drain-type vortexes. However, single-phase models cannot simulate stable drain-vortexes.

Keywords: CFD, SFR, gas entrainment, experimental validation

1 Introduction

ASTRID (Advanced Sodium Technological Reactor for Industrial Demonstration) was proposed by CEA (Commissariat à l'énergie atomique et aux énergies alternatives) as a prototype 4th generation 600 MW sodium-cooled fast breeder reactor (SFR). The pool-type reactor was close to the end of the conceptual design phase when it was stopped in 2018. Thermal hydraulics was recognized as one of the key scientific areas in the development of SFRs as ASTRID. Accurate knowledge of the velocity and temperature fields is needed for both nominal operation and accident sequences to allow technical and economic progress to be made in terms of increased compactness and safety, as well as decreased cost. In thermal-hydraulic studies related to a new reactor concept with reduced power (New-ASTRID), scaled experiments and detailed Computational Fluid Dynamics (CFD) simulations are used at CEA for the conception and design of the reactor vessel, for which three-dimensional flow effects may occur. The good knowledge of the flow fields in the upper plenum (also called hot pool) is of particular interest in this context and here especially the profound understanding of the mechanisms that might lead to gas entrainment into the reactor core. The use of CFD in the licensing process of the reactor is under discussion (Ferreri, 2014; Höhne et al. ,2018) .

Tenchine (2010) has reported an overview of the thermal-hydraulic challenges in SFRs. A possible limitation in the use of CFD is the state of validation of the codes due to the lack of appropriate validation experiments at a small scale. Nevertheless, a good database is available to establish correlations and to analyze global thermal-hydraulic effects in reduce scale mock-ups. Very early experiments in a 1/15th scale mockup of the Super-Phénix reactor were reported by Grand et al. (1979). Within the European fast breeder reactor (EFR) program (Lefevre et al., 1996), experiments were conducted at 1/20th scale in the RAMONA facility to study decay heat removal (Hoffmann, 1989). A larger water model at 1/5th scale called NEPTUN was also used to estimate the scale effect on the results to enable a better extrapolation to reactor scale (Hoffman et al., 1994; Weinberg et al., 1996). Marth (1993) summarized the history of the EFR Cooperation. Rodriguez et al. (2015) presented the qualification program of the ASTRID SFR project, including a picture of the EFR hot pool mock up COLCHIX. The MICAS experiments at CEA (Guenadou et al., 2016) were dedicated to

analyze the thermal hydraulic behavior in the hot pool of ASTRID. The main objective of the experiments was to establish a high fidelity database for CFD validation. Particular interest was on the risk of gas entrainment into the reactor core. More information on the MICAS program and the MICAS facility is given in section 5.

Tenchine et al. (2014) gave a detailed overview of the problem of gas entrainment in SFRs. Gas entrainment in the primary circuit of SFRs may lead to safety problems in case of accumulation and transport of larger pockets of gas through the core (Tenchine et al., 2014). A positive void reactivity effect could occur if gas is crossing the central part of the core. Moreover, the heat transfer efficiency of the coolant will be drastically reduced in sub-assemblies if the void fraction is significantly increased, leading to possible clad melting of fuel pins.

Various authors have reported basic experimental studies on gas entrainment in reactor pools. According to Satpathy (2012), four types of gas entrainment mechanisms are possible: vortex activated entrainment, liquid fall induced entrainment, entrainment due to the formation of a drain-type vortex (bathtub vortex) and entrainment due to shearing of gas-liquid interface. During the EFR project, the risk of entrainment of gas from the gas/liquid interface (free surface) into intermediate heat exchangers (IHX) via drain-type vortexes was detected, which is related to the higher compactness of this reactor concept compared to previous reactors (Tenchine, 2010). Hydraulic tests performed on water facilities showed that numerous vortices could be generated inducing bubbles entrainment in the main flow. Special devices were studied to completely avoid or at least to limit gas entrainment (Tenchine, 2010).

Numerous small-scale experiments exist to analyze the formation of drain vortexes. The setup ranges from simple, transient cylinder drain experiments (Park and Sohn, 2011) over steady state experiments in cyclone geometry (Monji et al., 2010; Moriya, 1998) to larger, steady state, drain experiments (Cristofano and Nobili, 2015). For example, Park and Sohn, (2011), Škerlavaj et al. (2010) and Merzari et al (2009) have numerically analyzed this type of experiments by using various modelling hypothesis for the free surface and turbulence treatment. Issa (2010) has investigated experimentally and numerically the influence of the geometry of the water-pump sump (pool geometry) and the inlet suction pipe on the flow field near pump intakes. This study also addressed gas entrainment by using single-phase modelling. Surface swirls in more dynamic flow, including vortex shedding, was studied in the BANGA experiments of CEA (Moudjed et al. 2016). Ito et al. (2010) summarized an overview of the gas entrainment activities of the Japanese Atomic Energy Agency. A CFD based method to predict the risk of gas entrainment was developed and validated by both small-scale experiments (e.g. the experiment of Monji et al. (2004)) and SFR related geometry as e.g. the $1/1.8^{th}$ scale partial model of the hot pool of a SFR (Kimura et al., 2008). Cristofano et al. (2015), however, tested the proposed method without success. Further, the authors did not succeed to apply the method proposed by Kimura et al.(2008) and Ito et al.(2010) to the BANGA experiment of Moudjed et al.(2016).

Due to the request of safety authorities to estimate the risk of gas entrainment into the reactor core of SFRs via drain vortexes that can be created by the intermediate heat exchangers in compact reactor designs, a fundamental CFD study has been launched at CEA. This study is based on the findings concerning the formation of surface swirls and gas drain vortexes, which were observed during the MICAS experimental study. After describing the numerical model in section 2, basic considerations of the pressure course in surface vortexes are presented in section 3 based on the example of the Rankine-vortex. Regarding the possible prediction of gas entrainment by CFD, in section 4 fundamental tests on swirling flow are discussed. On the example of a single vortex experiment, the CFD model is analyzed with respect to turbulence modelling, numerical schemes and mesh types. Finally, in section 5, results of the analysis of the flow in MICAS facility are presented. In this facility, two types of intermediate heat exchanger operation are analyzed: all four heat exchangers in operation and two out of four heat exchangers in operation. The first configuration is used for code validation purpose. In the second configuration, gas entrainment into the IHX intakes was observed experimentally. The flow fields calculated by RANS and LES are compared and particularities regarding the instantaneous pressure distribution close to the IHX are discussed.

2 The numerical model

The analysis presented here was performed with TrioCFD (Angeli et al., 2015), the general CFD code developed at CEA-Saclay, which is available as Open Source. First, the conservation equations with the main assumptions are presented and then the numerical scheme is discussed. The fluid is assumed incompressible and Newtonian. Buoyancy effects due to the dependency of the density (ρ) on the temperature (T) are not taken into account. Dependent on the physical requirements of the studies presented, turbulence is treated either with Reynolds Averaged Navier-Stokes (RANS) equations or with Large Eddy Simulations (LES).

For LES, a filtering operation is applied on the conservation equations for mass and momentum. The instantaneous, filtered velocity $\tilde{u}$ is defined by the equations of mass conservation (eq.(1)) and momentum conservation (eq.(2)). Einstein's notation is used.

$$\frac{\partial \widetilde{u_j}}{\partial x_j} = 0 \ , \tag{1}$$

$$\frac{\partial \widetilde{u_i}}{\partial t} + \frac{\partial (\widetilde{u_i}\,\widetilde{u_j})}{\partial x_j} = -\frac{\partial \widetilde{P_h}}{\rho \partial x_i} + \frac{\partial}{\partial x_j}\left[\frac{\mu}{\rho}\left(\frac{\partial \widetilde{u_i}}{\partial x_j} + \frac{\partial \widetilde{u_j}}{\partial x_i}\right) - \tilde{\tau}_{ij}\right] \ . \tag{2}$$

P_h is the hydraulic pressure and μ the dynamic viscosity. The sub-grid-scale stress tensor τ_{ij} is defined as:

$$\tilde{\tau}_{ij} \equiv \left(\widetilde{u_i u_j} - \widetilde{u_i} \cdot \widetilde{u_j}\right) = \frac{\partial}{\partial x_j}\left[\frac{\mu_{SGS}}{\rho}\left(\frac{\partial \widetilde{u_i}}{\partial x_j} + \frac{\partial \widetilde{u_j}}{\partial x_i}\right)\right] + \frac{1}{3}\tilde{\tau}_{kk}\delta_{ij} \ . \tag{3}$$

The wall adaptive, local eddy-viscosity model (WALE) of Nicoud and Ducros (1999) is applied to calculate the sub-grid-scale viscosity μ_{SGS} according to the following equations (C_w=0.5):

$$\frac{\mu_{SGS}}{\rho} = (C_w \overline{\Delta})^2 \frac{\left(s_{ij}^d \cdot s_{ij}^d\right)^{3/2}}{\left(S_{ij} \cdot S_{ij}\right)^{5/2} + \left(S_{ij} \cdot S_{ij}\right)^{5/4} + 10^{-6}} \tag{4}$$

with

$$S_{ij} = \frac{1}{2}\left(\frac{\partial \tilde{u}_i}{\partial x_j} + \frac{\partial \tilde{u}_j}{\partial x_i}\right) \qquad \text{and} \qquad s_{ij}^d = \frac{1}{2}\left(\left(\frac{\partial \tilde{u}_i}{\partial x_j}\right)^2 + \left(\frac{\partial \tilde{u}_j}{\partial x_i}\right)^2\right) - \frac{1}{3}\left(\frac{\partial \tilde{u}_i}{\partial x_i}\right)^2 \cdot \delta_{ii} \tag{5}$$

For RANS, the Reynolds averaging procedure is applied on the instantaneous velocity, which is decomposed into a statistical mean value $\bar{u}$ and a fluctuating component u'. The mean velocity is determined by the equations of mass conservation (eq.(6)) and momentum conservation (eq.(7)).

$$\frac{\partial \overline{u_j}}{\partial x_j} = 0 \ , \tag{6}$$

$$\frac{\partial \overline{u_i}}{\partial t} + \frac{\partial (\overline{u_i}\,\overline{u_j})}{\partial x_j} = -\frac{\partial \overline{P_h}}{\rho \partial x_i} + \frac{\partial}{\partial x_j}\left[\frac{\mu_{RANS}}{\rho}\left(\frac{\partial \overline{u_i}}{\partial x_j} + \frac{\partial \overline{u_j}}{\partial x_i}\right) - \bar{\tau}_{ij}\right] \ . \tag{7}$$

Applying the Boussinesq hypothesis, the Reynolds stress tensor τ_{ij} is defined according to:

$$\bar{\tau}_{ij} \equiv -\overline{u_i' u_j'} = \frac{\mu_{RANS}}{\rho}\left(\frac{\partial \overline{u_i}}{\partial x_j} + \frac{\partial \overline{u_j}}{\partial x_i}\right) - \frac{2}{3 \cdot \rho} k \delta_{ij} \tag{8}$$

For the statistical turbulence model, the following formulation of the k-ε model is used (Pope, 2000):

$$\frac{\partial k}{\partial t} + \frac{\partial (\overline{u_j} k)}{\partial x_j} = \frac{\partial}{\partial x_j}\left[\left(\frac{\mu}{\rho} + \frac{\mu_{RANS}}{\rho \cdot \sigma_k}\right)\frac{\partial k}{\partial x_j}\right] - \varepsilon + P \quad , \tag{9}$$

$$\frac{\partial \varepsilon}{\partial t} + \frac{\partial (\overline{u_j} \varepsilon)}{\partial x_j} = \frac{\partial}{\partial x_j}\left[\left(\frac{\mu}{\rho} + \frac{\mu_{RANS}}{\rho \cdot \sigma_\varepsilon}\right)\frac{\partial \varepsilon}{\partial x_j}\right] + C_{\varepsilon 1} P \frac{\varepsilon}{k} - C_{\varepsilon 2}\frac{\varepsilon^2}{k} \tag{10}$$

with $\qquad \frac{\mu_{RANS}}{\rho} = c_\mu \frac{k^2}{\varepsilon} \qquad$ and $\qquad P = -\overline{u_i' u_j'}\frac{\partial \overline{u_i}}{\partial x_j}$

The Reynolds stresses $\overline{u_i' u_j'}$ of the production term P are calculated from eq.(8). The following empirical coefficients are used: $c_\mu = 0.09$, $\sigma_k = 1$, $\sigma_\varepsilon = 1.3$, $C_{\varepsilon 1} = 1.44$ and $C_{\varepsilon 2} = 1.92$.

Non-slip walls enclose the calculation domain. Wall functions are used to model momentum exchange between walls and fluid. For LES and RANS, the general wall law of Reichardt (Reichardt, 1951) is applied that spans with one correlation the three sublayers of viscous-, buffer- and logarithmic law region (κ=0.415). The correlation is written for the non-dimensional velocity U^+:

$$U^+ = \frac{U}{U_\tau} = \frac{1}{\kappa} \cdot \ln(1 + \kappa \cdot y^+) + 7.44 \cdot \left(1 - e^{(-y^+/11)} - \frac{y^+}{11} e^{(-y^+/3)}\right) \quad (11)$$

U_τ and y^+ are friction velocity and non-dimensional wall distance, respectively. Definitions of all non-dimensional quantities can be found in Pope (2000). In RANS modelling, local equilibrium between production and dissipation of turbulent kinetic energy is assumed at the first near wall calculation point. The following boundary conditions for k and ε are derived from Reichardt's wall law (eq.11). The functions are written in non-dimensional form:

$$k^+ = \frac{k}{{U_\tau}^2} = 0.07 \cdot {y^+}^2 \cdot e^{\left(-\frac{y^+}{9}\right)} + \frac{1}{\sqrt{c_\mu}} \left(1 - e^{\left(-\frac{y^+}{20}\right)}\right)^2 \quad (12)$$

$$\varepsilon^+ = \frac{\varepsilon}{\nu {U_\tau}^4} = \frac{1}{\kappa \cdot \left({y^+}^2 + 15^4\right)^{\frac{1}{4}}} \quad (13)$$

At inflow faces, Dirichlet boundary conditions with imposed velocity are used. In this context, k and ε were calculated from a spatial mean velocity $|U_m|$ and a hydraulic diameter d_h (Beck et al. 2017), assuming a turbulence level of X %:

$$k = \frac{1}{2} \cdot (u')^2, \qquad \varepsilon = \frac{{c_\mu}^{3/4} \cdot k^{3/2}}{d_h} \quad \text{and} \quad u' \approx 0.01 \cdot X \cdot |U_m| \,. \quad (14)$$

(14)

Neumann boundary conditions with imposed pressure are used at outflow faces. Free surfaces are modeled as inviscid planes called free slip walls or symmetry planes.

TrioCFD uses a finite volume based finite element discretization method on tetrahedral cells to integrate in conservative form all conservation equations over the control volumes belonging to the calculation domain. As in the classical Crouzeix–Raviart element (Crouzeix and Raviart, 1973), both vector and scalar quantities are located in the center of the faces. The pressure, however, is located in the vertices and the center of gravity of a tetrahedral element (Angeli et al, 2018). This discretization leads to a very good pressure/velocity coupling and has a very dense divergence free basis. Along this staggered mesh arrangement, the unknowns, i.e. vector and scalar values, are expressed using non-conforming linear shape-functions (P1-non-conforming). The shape function for the pressure is constant for the center of the element (P0) and linear for the vertices (P1).

For LES, the second order explicit Adams-Bashforth scheme is used for time integration. The time-step respects the Courant-Friedrichs-Levy stability criteria (CFL) with CFL<0.8. A slightly stabilized second order centered convection scheme is applied. The diffusion term is discretized by a centered second order scheme. For RANS calculations, the second order backward implicit scheme is used for time integration. This scheme ensures good stability during the transient. A second order convection scheme of MUSCL type is applied. The diffusion term is discretized by a centered scheme of second order. The numerical schemes that are used for the MICAS studies are summarized in Table 1 for LES and RANS. The discretized momentum conservation equations are solved following the SOLA pressure projection method (Bieder et al, 2018). The resulting Poisson equation is solved with a conjugate gradient method using a symmetric successive over relaxation technique to improve convergence. The convergence threshold has been set to 10^{-8} for all calculations presented here.

Table 1: Summary of the numerical scheme for the MICAS calculations

	RANS	**LES**
Meshing		
Mesh type	Tetrahedrons	Tetrahedrons
Mesh number	14×10^6	40×10^6
Refinement	Following BPG	Respecting Taylor scale
Numerical scheme		
Time integration	2nd order implicit	2nd order explicit
Convection	2nd order upwind	2nd order centered
Diffusion	2nd order centered	2nd order centered
Pressure gradient	1st order	1st order
Turbulence treatment		
Turbulence model	High Re k-ε	WALE
Wall treatment	Reichardt's law	Reichardt's law
First near wall point y^+	40 to 100	10 to 40

3 Rankine-vortex: a simple vortex model

As first step of the study, the horizontal pressure distribution in a simple vortex is discussed. Many single-cell, axisymmetric, Newtonian-fluid, swirling vortex flows models have been developed over the years. Rodriguez et al. (2012) give an overview over 13 more or less popular models. The Rankine-vortex (Rankine, 1858) is the most simple and idealized of such vortex models. The model is a solution of the Euler equations and consists of a cylindrical, rigid, central vortex of the radius a, which rotates with a constant angular velocity w. This inner vortex is surrounded by a free, inviscid outer vortex. The tangential, circular velocity v_Θ at radius r is defined as:

$$v_\theta = \begin{cases} wr, & for\ r < a \\ \frac{wa^2}{r}, & for\ r > a \end{cases} \tag{15}$$

The steady state solution of the Euler equations leads to the following pressure field as function of density ρ, radius r and axial location z (depth) and gravitational acceleration g:

$$P(r,z) = \begin{cases} +\rho w^2 \frac{r^2}{2} - \rho g z, & for\ r < a \\ -\rho w^2 \frac{a^4}{2r^2} - \rho g z + \rho w^2 a^2, & for\ r > a \end{cases} \tag{16}$$

A continuous pressure at the radius a = 0.005 m is assumed. Radial profiles of the circular velocity and the pressure are shown in Fig.1 for an angular velocity of w = 35 1/s and a depth of z = 0.01m. The fluid is water with ρ = 1000 kg/m^3. It is interesting to note that the pressure course and thus the pressure difference between the center of the vortex and a location far from the center is density independent. The axial location of the vortex (depth z) only adds a constant shift to the pressure profile. Such a vortex might be calculated by single phase CFD.

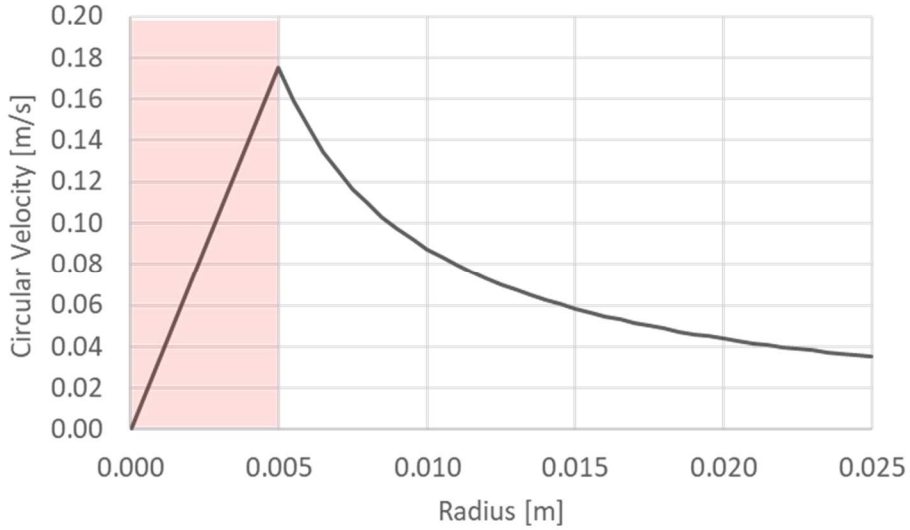

a) Velocity profile of the Rankine-vortex

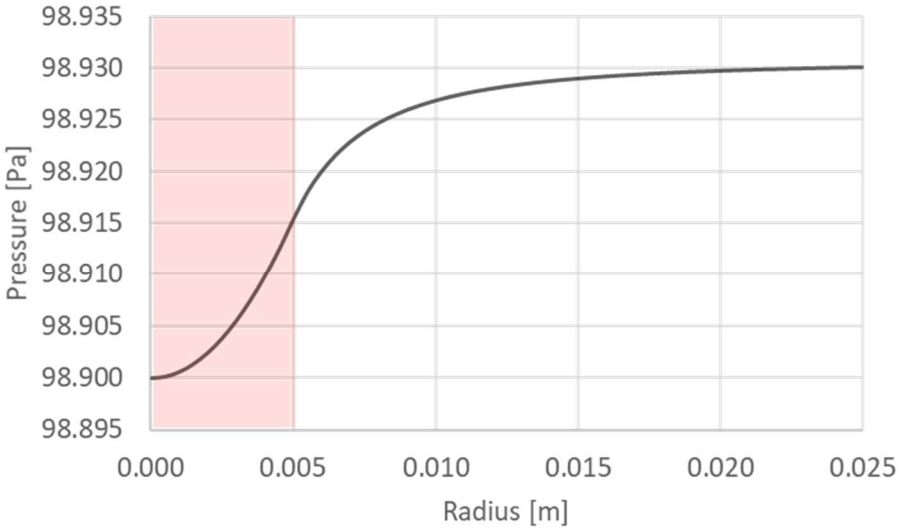

b) Pressure profile of the Rankine-vortex

Fig.1: Rankine-vortex; tangential velocity in a) and pressure profile in b)

The Rankine vortex shown in Fig.1 was defined for a single-phase fluid of constant density ρ, located in depth z below the liquid surface. Fig.2a shows in a schematic way a two-phase flow vortex. In depth z, the pressure in the liquid phase at the interface between gas and liquid is balanced by the centrifugal force of the rotating vortex. In analogy to eq.(2), the steady state solution of the Euler equation is given in eq.(3):

$$P(r,z) = \begin{cases} +\rho_g w^2 \frac{r^2}{2} - \rho_g g z & for\ r < a \\ -\rho_l w^2 \frac{a^4}{2r^2} - \rho_g g z + (\rho_g + \rho_l) w^2 \frac{a^2}{2} & for\ r > a \end{cases} \quad (17)$$

A reduction of the pressure difference at the interface due to the surface tension is not taken into account. A continuous pressure at the gas/liquid interface at radius a =0.005 m is assumed. An example of the radial pressure profile for a fictive gas/liquid couple is shown in Fig.2b. Gas and liquid densities are 1 kg/m^3 and 1000 kg/m^3, respectively. The profile is calculated for a depth of z = 0.1 m.

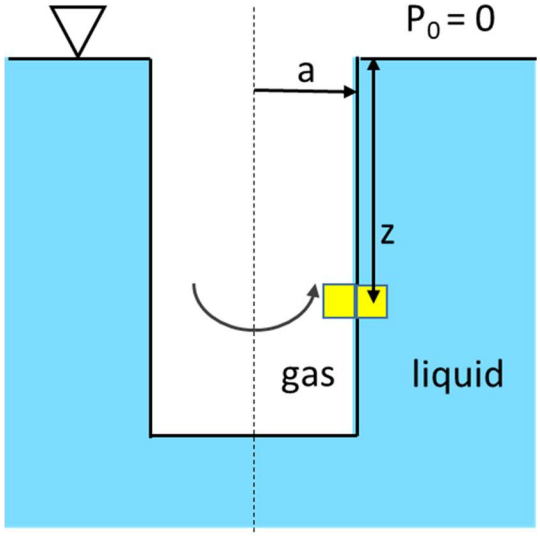

a) 2 phase Rankine-vortex

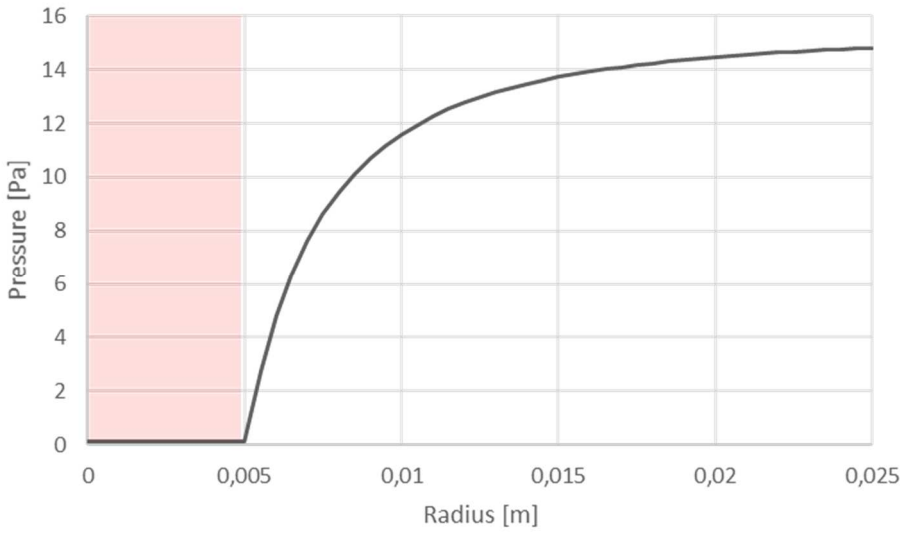

b) Pressure profile of a two-phase Rankine-vortex

Fig.2: Two-phase Rankine-vortex; physical model in a) and pressure profile in b)

It is evident that the radial pressure course and in particular the pressure difference between gas core and liquid is a function of the density difference. In fact, the total pressure difference of the two-phase model exceeds significantly that of the single-phase model (see Fig.1b). In presence of gravitational forces, the horizontal pressure difference between gas core and liquid phase increases with depth as function of the gas density. If the gas vortex starts to incline from the vertical axis, gravitation will push back the vortex to its vertical orientation what stabilizes the vortex along its rotational axes. The deeper the gas core enters into the liquid, the higher the rotational velocity to counterbalance the increased static pressure. Surface tension with the associated surface curvature will increase the pressure in the gas phase what will reduce the effect of stabilizing the gas core. In summary, close to the surface and far from intakes, the rotational axis of the gas core of an entrainment vortex is aligned predominantly in direction of the gravitational force. Close to the intakes, the gas core can be inclined out of the rotational axis.

This simple comparison of the results of Rankine-vortexes already demonstrates the difficulty in estimating the risk of gas entrainment by single-phase considerations as the effect of the gas core on

the pressure field in the liquid cannot be taken into account in this kind of modelling. Simulating rotational flow by CFD is another challenge in the prediction of gas entrainment. This aspect will be treated in the following section.

4 Calculating swirling flow

Two challenging points in analyzing the risk of drain swirls numerically exist for the mesh generation: on the one hand, the small diameter of the entrainment swirl and on the other hand the observation that this swirl can meander around in a larger zone of the free surface. It is not possible in engineering investigations to mesh this zone sufficiently fine to capture correctly the swirl with approximately 15 to 20 calculation points per swirl diameter. Concerning turbulence modelling, swirling flow is a typical example for anisotropic turbulence; the uses turbulence model must thus account for this effect. Hence, as preparatory study, the capability of various numerical approaches was tested to calculate entrainment vortexes with a mesh refinement that is typical for thermal hydraulic studies in SFR hot pool studies. For this separate effect study, the small-scale experiment of Monji et al. (2004) has been selected as test case.

4.1 Experimental set-up of the Monji experiment

Monji et al. (2004) have described their air entrainment experiment in the following way. The experimental apparatus was a simple loop consisting of a cylindrical test section, a rectifier of water, a pump and an electromagnetic aerometer. The test section was a cylindrical vessel of 0.20 m inner diameter D. The water was fed to the vessel until a certain depth of the water was reached in the test section. In the analyzed experiment, the water depth H was kept constant at 0.25 m. The pump drove the water, which flowed to the test section through the rectifier. The inlet part was a rectangular channel that has a width e of 0.02 m. The water flowed into the test section along the tangential direction of the wall through the rectangular channel. Therefore, the water flowed circularly in the vessel. The outlet pipe of 0.015 m inner diameter d was connected in the center of the bottom plate of the cylindrical vessel. The water flowed out from this outlet pipe. Therefore, in the test section, circulation and downward flow of the water was observed. The water flowed through the electromagnetic aerometer connected to the outlet pipe and returned to the pump. The test section, rectifier and bottom plate made of a transparent acrylic resin to observe the flow. The water flow rate could be controlled at every 0.1s. The minimal step controlling the flow rate was 0.1 l/min. The test section as used in this study is shown in Fig.1. The cylindrical vessel as well as tangentially connected rectangular inlet channel and outlet tube are well visible and the main length are summarized.

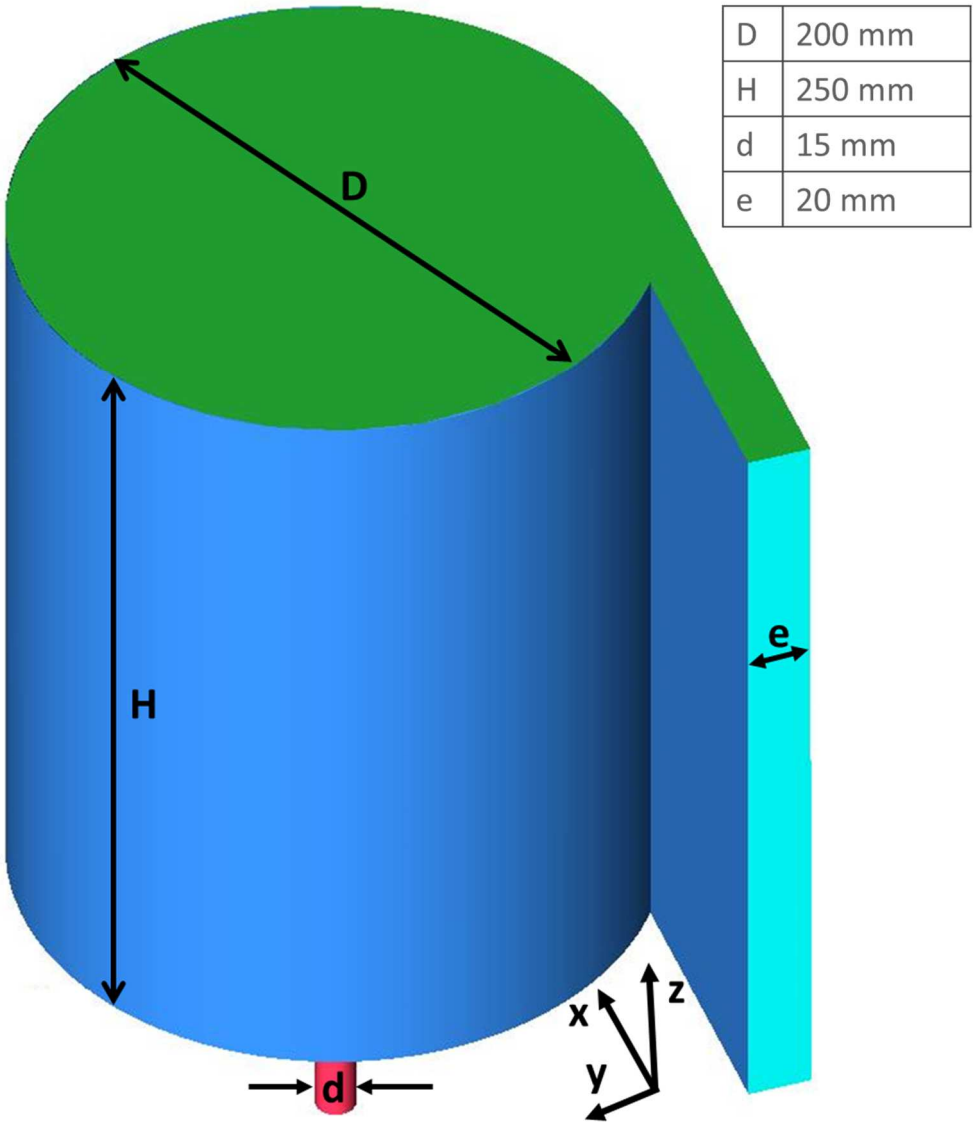

D	200 mm
H	250 mm
d	15 mm
e	20 mm

Fig.3 Scheme of the Monji experiment with test section, tangentially connected rectangular inlet channel and outlet tube

4.2 CAD model and meshing

The CAD model was built in SALOME[1] platform and was transferred in STEP format to the commercial mesh generator ICEMCFD. A pure tetrahedral meshing was created by using the Delaunay method. This meshing contains 620,000 tetrahedrons. The tetrahedrons in the rectangular inlet channel and the cylinder have the same size with about 1.2 mm distance between adjacent velocity points. The outlet tube was discretized with a refinement factor of 0.5. Prismatic near wall meshes to better resolve boundary layers were not introduced since the analysis of the central vortex is the objective of the study. The resulting surface meshing is shown in Fig.4.

[1] https://www.salome-platform.org/

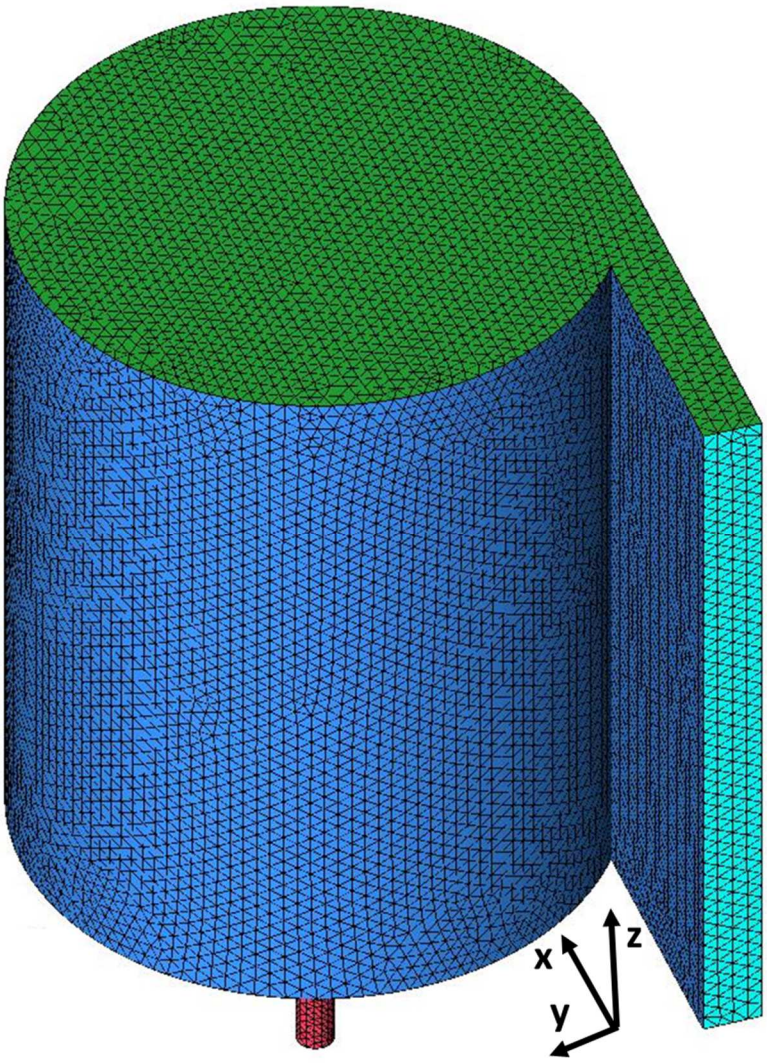

Fig.4 Meshing of the Monji experiment

4.3 CFD-analysis of an experiment

The fluid is water at ambient temperature (ρ = 1000 kg/m^3, μ = 0.001 Pa·s). A test case with a water flow rate of 0.1 l/s was selected, in which a gas core did not develop in the central vortex and the observed free surface was almost plane. Nevertheless, a central vortex develops, for which measurements of the tangential velocity exist (Sakai et al., 2008). Since an air core did not develop at these low velocities, the formation of the central vortex can be calculated with single-phase models. Reynolds number calculated for the rectangular inlet channel is about Re = 200.

4.3.1 Laminar Flow

Due to the low Reynolds number, laminar flow hypothesis was used for this first calculation. In Fig.5a, the norm of the circular, tangential velocity is shown in color scale in a plane that cut at z = 0.15 m horizontally across the cylindrical test section. The vectors indicate the direction of the flow. A temporal mean value was calculated over about five turnover cycles. The maximum value of the circular velocity with about 0.09 m/s is calculated close to the vortex axis at about r = 0.01 m, due to the conservation of the angular moment. A radial profile of the calculated circular velocity is compared in Fig.5b to the corresponding measurement. The line in Fig.5a shows the location of the profile. The good agreement between calculation and measurement is well visible. This result shown the good performance of the numerical scheme of TrioCFD for laminar flow, especially that the discretization on tetrahedral cells does not degenerate the velocity profile.

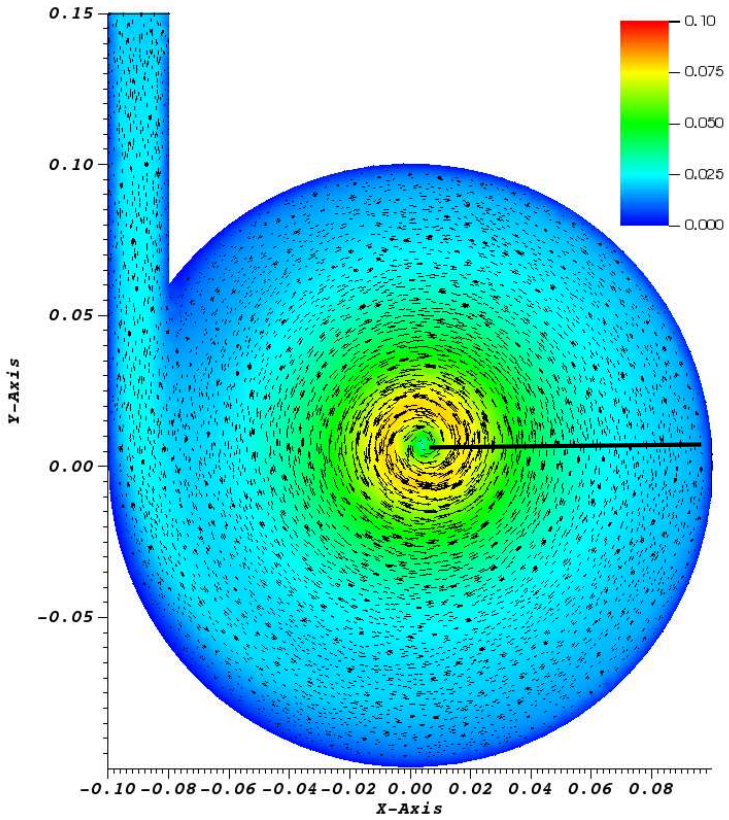

a) Distribution of the mean circular velocity

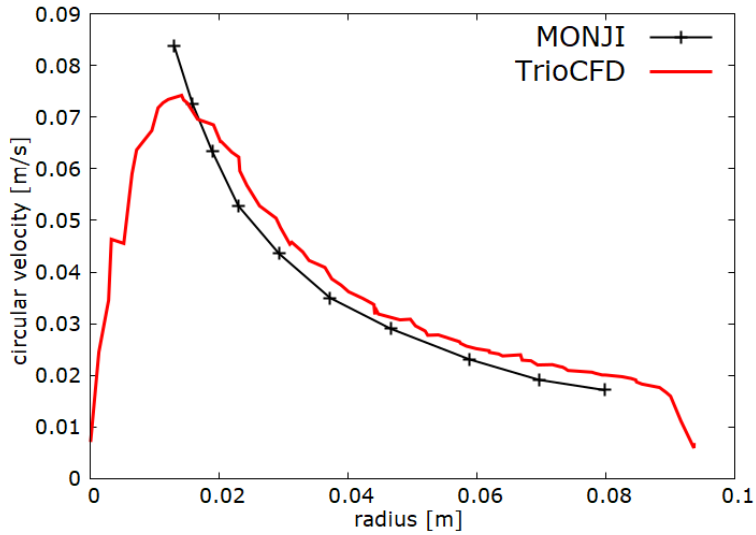

b) Radial profile of the mean circular velocity

Fig.5 Monji experiment: a) spatial distribution of the mean circular velocity at z=0.15 m and b) comparison of the calculated and measured radial profile of the circular velocity.

The Reynolds number calculated for the outlet tube is approximately Re= 16,500 (outlet velocity about 1.1 m/s). It was thus tested how LES and linear RANS models will influence the calculated distribution of the circular velocity in the test section.

4.3.2 LES analysis

In LES, in the whole calculation domain, the calculated turbulent viscosity was smaller than the viscosity of the fluid with the exception of the outlet tube and the center of the swirl. Only in these locations, the turbulent viscosity exceeds the molecular viscosity of the fluid slightly. Hence, LES leads in the cylindrical test section to the same velocity distribution as shown in Fig.5 for the laminar calculation.

4.3.3 RANS modelling

For RANS modelling, the high Reynolds k-ε model with wall function was tested to reproduce the central vortex of the Monji et al. (2004) experiment. It is well known that linear RANS models cannot reproduce correctly swirling flow. Nevertheless, it is important to understand how these models degrade the calculated flow field. Non-linear RANS models were not tested as these models might lead in complex flow conditions to unphysical results (Bieder, 2012). Therefore, in the near future, this model type might not be used in safety analysis at CEA.

At the inlet faces, flow with low turbulence intensity was simulated with k = 0.001 m^2/s^2 and ε = 0.01 m^3/s^3. Fig.6 shows in color scale the norm of the circular velocity in a plane that cut at z = 0.15 m horizontally across the cylindrical test section. The vectors indicate the direction of the flow. Fig.6 shows that the RANS model certainly calculates the formation of a swirl. The maximum of the circular velocity is at about 0.3 m/s. This maximum is located at a radial distance from the swirl center of about 2/3 of the cylinder radius (r ≈ 0.065 m). Comparing this flow field to the experimental finding shown in Fig.5 (maximum velocity of 0.09 m/s at r ≈ 0.1 m), it can be concluded that linear RANS indeed leads to swirl formation. However, the acceleration of the swirl close to the axis of the test section is not calculate correctly.

In order to assure that this behavior of the RANS model was not related to the discretization of TrioCFD, (staggered arrangement of velocity and pressure) the same calculation has been accomplished with the FLUENT code (co-localization of velocity and pressure). The identical meshing and the same boundary conditions were used. Without surprise, co-localized arrangement of unknowns predicted the identical flow behavior as staggered arrangement of unknowns. The comparison of the field of the norm of the circular velocity at z = 0.15 m is shown in Fig.6 for two arrangements of the unknowns. Ferziger and Peric (2002) discussed for instance staggered grid discretization and co-localized arrangement of unknowns. More information on the discretization of TrioCFD can be found in Angeli et al. (2018).

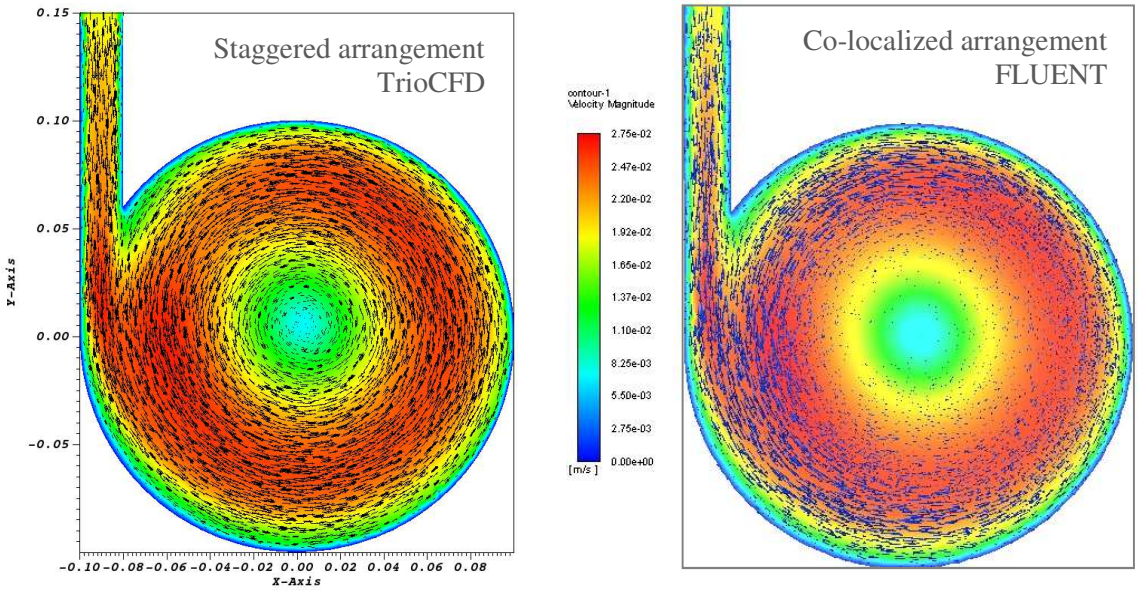

Fig.6 Monji experiment: spatial distribution of the mean circular velocity at z=0.15 m, calculated

with the high Reynolds number k-ε model implemented in TrioCFD and FLUENT

It is important to verify if other RANS models than the high Reynolds number k-ε model can reproduce the central vortex correctly when using the same mesh type and mesh size as before. Hence, for the experiment of Monji et al. (2004), the circular velocity of four calculations with different turbulence models were compared: laminar flow hypothesis, high Reynolds number k-ε model with standard coefficients, k-ε realizable model and k-ω SST model. The FLUENT code was used for this comparison. All calculations use the same meshing described in section 3. Unsteady calculations with the SIMPLE method were performed to solve the momentum equations. The residue of all unknowns converge below 10^{-4}, except for mass conservation where the residue could not descend below 10^{-2}. This comparison of instantaneous circular velocities is shown in Fig.7 for two planes, one cut horizontally at z = 0.15 m and one cuts vertically at y = 0 m.

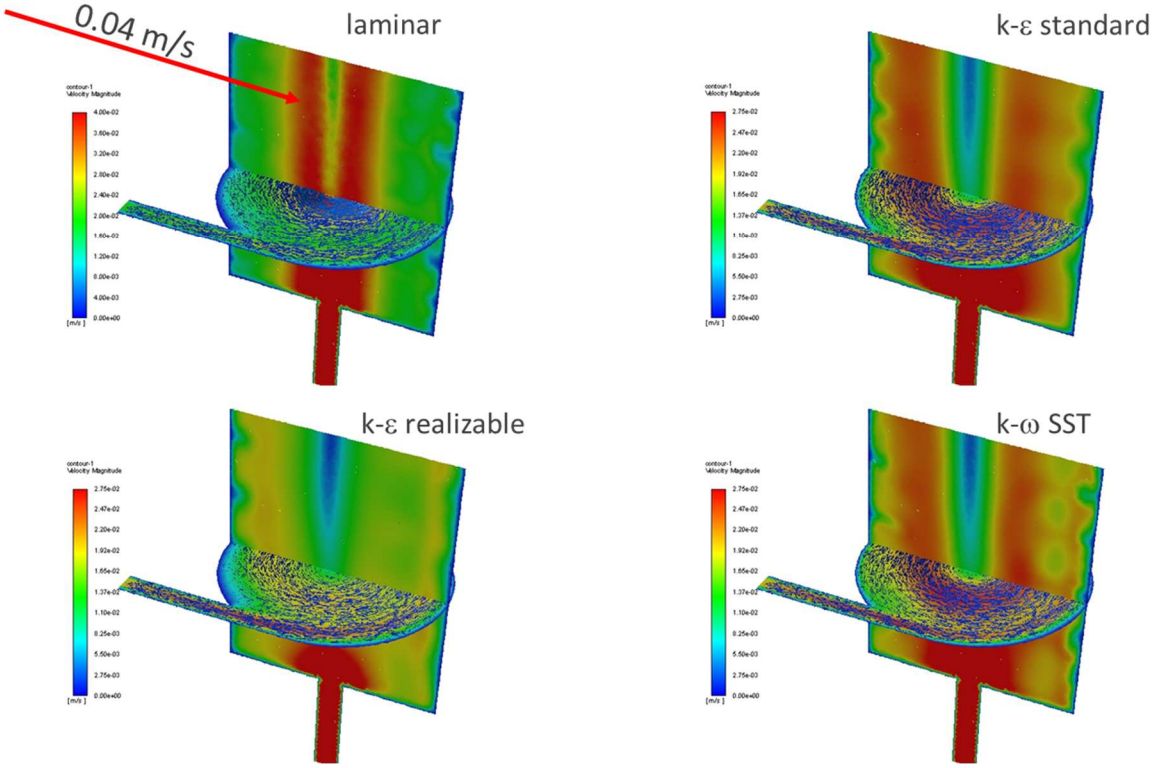

Fig.7 Comparison of the circular velocity: laminar flow hypothesis, high Re k-ε model with standard coefficients, k-ε realizable model and k-ω SST model

With laminar flow hypothesis, the circular velocity of the center vortex does not reach the experimental value of about 0.09 m/s. The calculated maximum circular velocity is about 0.04 m/s. With the used size and type of the mesh, it seems that the co-localization of unknowns does not allow representing correctly the circular flow in the center of the vortex. Test calculations with a block-hexagonal meshing of 1.3 million elements lead to the correct maximum circular velocity in the center of the vortex.

Not any of the linear RANS models is able to get correctly the fast rotating central vortex as calculated with the laminar hypothesis by staggered grid discretization (Fig.5). In all RANS calculations, the maximum circular velocity is located at about 2/3 of the radius of the cylindrical test section. This incapacity of the used RANS models to calculate correctly the central vortex is confirmed by Škerlavaj et al. (2010) who used SST based turbulence model (without further specification) with and without curvature correction.

Further FLUENT calculations have been performed to eliminate modelling effects that can lead to the wrong flow field: on the one hand, a block-hexagonal meshing of 1.3 million elements was used at Re = 200 to eliminate effects of the mesh type and on the other hand, a higher Reynolds number was chosen (Re = 3600) to eliminate Reynolds number effects. Both calculations confirmed the wrong location of the maximum circular velocity at a distance from the cylinder axis of 2/3 cylinder radius.

It is interesting to note that all linear RANS models predict secondary vortices that can be interpreted as Taylor vortices by using Taylor-Couette flow analogy (Mulligan et al. 2018). However, in the presented calculations, the driving internal maximum circular velocity is located unphysically close to the steady external cylinder wall. The annular flow analogy assumed by Mulligan et al. (2018) does probably not represent the reality in the setup of Monji et al. (2004), where the central vortex has a much lesser radius.

In conclusion, using tetrahedral meshes in combination with co-localized arrangement of unknowns, the entrainment swirl could not have been calculated correctly (with the used mesh refinement), neither with laminar flow hypothesis nor with linear RANS models. However, using tetrahedral meshes with staggered arrangement of unknowns, the swirl has been calculated correctly with laminar flow hypothesis and LES. Thus, all analyses of the MICAS experiments in in the next section were carried out on staggered grids with TrioCFD.

5 Studies of the flow in the hot pool of a prototype SFR

Although RANS did not calculate correctly the form of the entrainment swirl in a laboratory size experiment, it is not a priori evident that RANS cannot predict at all, the entrainment swirls in SFR hot pool geometry. Therefore, two MICAS experiments were analyzed with RANS and LES, one without gas entrainment for validation purpose and other one with gas entrainment.

5.1 Experimental set-up of the MICAS experiment

Guenadou et al. (2016) describe the MICAS facility in the following way. This 1/6th scale model of the ASTRID upper plenum was built in transparent polymer for optical visualizations. On the photo and the scheme of MICAS presented on the Fig.8 one can be distinguish the four intermediate heat exchangers (IHX) in the corners, the four direct heat exchangers (DHX), the above core structure (ACS) in the center just above the core, the three pump pits (P0), one decay heat exchanger (RR1a), and three inspection accesses during operation (ISIR).

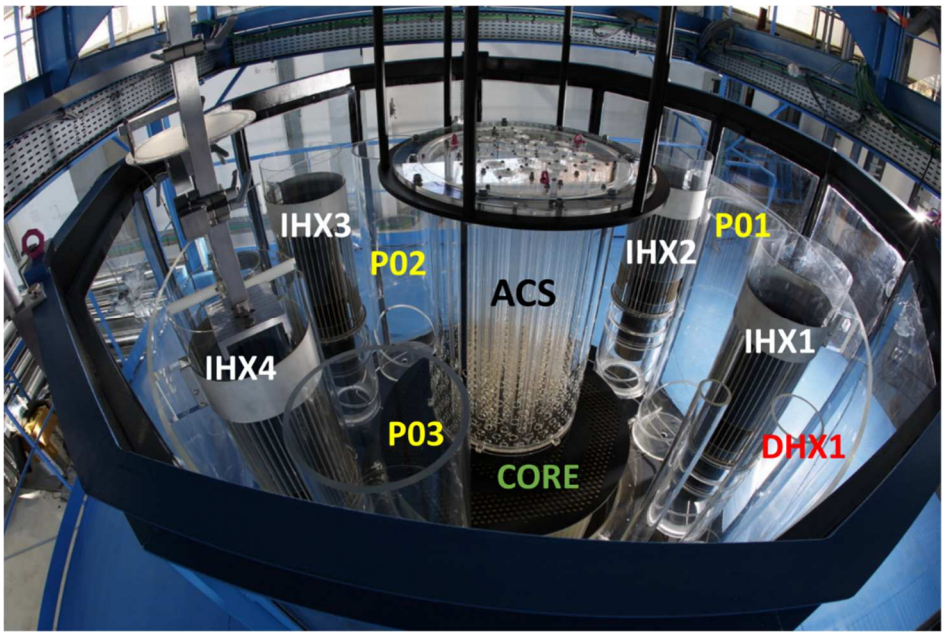

a) Perspective view on the MICAS facility

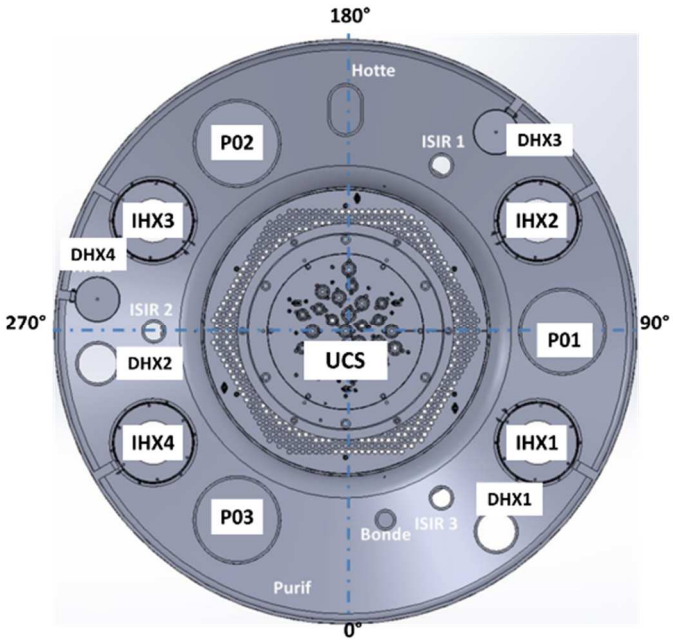

b) Location of internals

Fig.8: The MICAS facility; a) perspective view, b) location of the internals

The IHX geometry can be changed in terms of elevation and height of the opening. The upper plenum model is surrounded by a pool, which is built of 12 transparent planar walls. This pool is filled with water to limit optical deformations. The mock-up is supplied by the PLATEAU loop at a 380 m^3/h maximal flow rate. The core is split in three injection zones (Beck et al. 2017): the fission area, the reflectors and the internal fuel storage. In those zones, the flow rates are controlled according to the real flow distribution in SFR. Gueandou et al. (2015) describe the PLATEAU facility in detail. The following quantities are measured during the first hydraulic measuring campaign (Guenadou et al, 2017):

- Velocity fields in various vertical plans in the hot pool (particularly around ACS and IHX) by using PIV techniques. The acquisition rate is 15 Hz (integration time is 10 s). The error of the measured velocities has been evaluated to be about 1%. The laser planes are positioned with an error of ±1°.
- Water injection flow rates in the three core regions, measured by three Coriolis flowmeters with an accuracy of 0.1%;
- Location of the water level above the core outlet plate, measured with an accuracy of +/- 2 mm;
- Flow rate entering the ACS measured by integrating the measured velocity fields along the inlet of the ACS as well as at the ACS barrel holes (accuracy below 10%).

5.2 CAD model and meshing

The geometrical model and the meshing of the MICAS facility have been optimized step by step in order to achieve convergence of the calculated flow field on mesh refinement. Bieder et al. (2019) described this process in detail. PYTHON scrips have been developed in SALOME platform to accelerate and control the optimization process. The CAD model has been improved successively and the design of the model becomes more and more realistic. The use of pressure loss correlations to represent small geometrical features of the facility has been avoided where possible.

The final geometrical model and an example of the meshing is shown in Fig.9 for a vertical plane that cut for an azimuthal angle of 54° through IHX1 and IHX3 (28 million tetrahedrons). The free surface is set in all calculations presented here at a height of 1.425 m that is 0.786 m above the core outlet plate. Solid walls are shown as red lines.

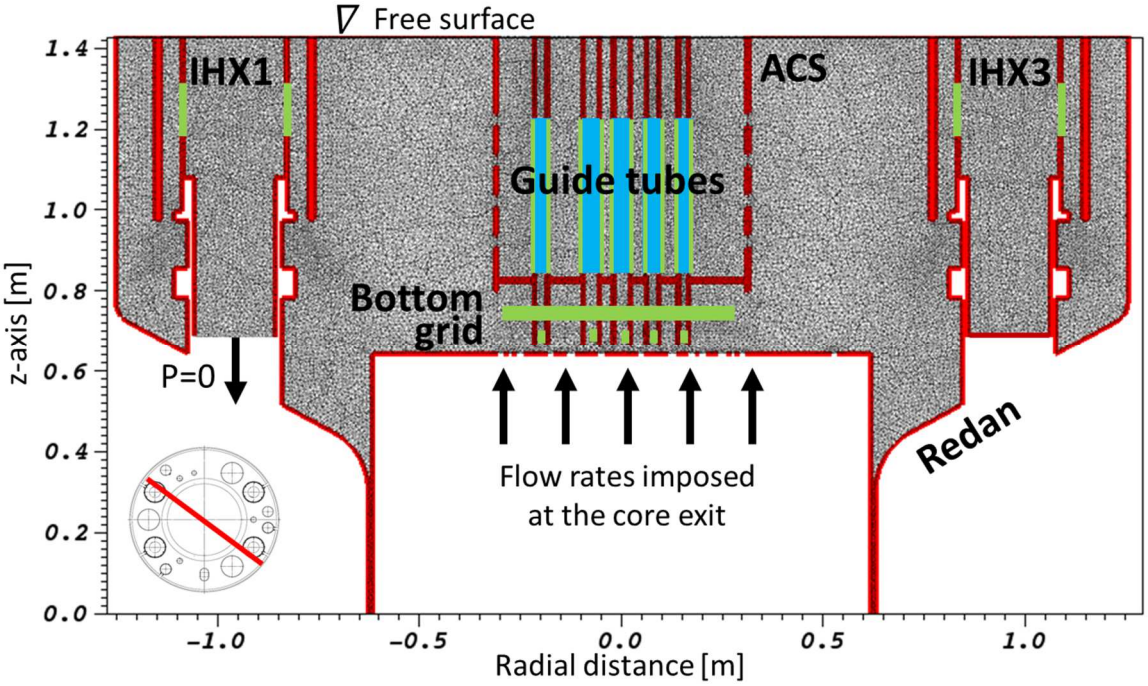

Fig.9 Meshing and modelling of the above core structure

Very small geometrical features are modeled by local pressure drop coefficients that have been taken from Idel'cik (1969). Their locations are shown as green lines. They represent the bottom grid (circular perforated plate), the perforated sections of guide tubes and the inlet structures of the IHXs. The reduction of the flow area in the guide tubes due to the presence of control rods is modeled by means of porosities (blue zones in Fig.9) and local pressure drop coefficients at the inlet of the guide

tubes in order to simulate the resulting sudden contraction of the flow area. The flow holes in the ACS are explicitly meshed.

The working fluid is water at 22°C with constant physical properties. Dirichlet boundary conditions were used at the core exit as the core outlet plate represents the inlet plane of the calculation domain. For each assembly outlet, constant values of the mean velocity as well as of k and ε were imposed. Neumann boundary conditions are applied at the outflow faces of the IHXs with an imposed constant pressure for the momentum equations (same pressure at open IHXs) and free outflow conditions for k and ε. The water surface is modeled with symmetry conditions as free-slip wall.

More information on the meshing for RANS is given in section 5.3.1. In this section, the validation of the model for RANS calculations is also presented. For LES, the meshing should respect the criteria of the Taylor micro scale d_t. The Taylor micro scale is estimated for the complete calculation domain from eq.(18) according to:

$$d_t \approx \sqrt{10 \cdot \nu \cdot k/\epsilon} \tag{18}$$

The quantities k and ε were taken from the corresponding RANS calculation. More information on the meshing for LES is given in section 5.3.2.

5.3 Numerical analysis of the flow in the MICAS facility

The MICAS experiment was analyzed for two conditions of IHX operation: normal operation with all four IHXs in operation and accidental operation with two out of four IHXs in operation. The first case is used as reference case and for validation of the RANS model, especially concerning the flow field near the heat exchanger's intake. In the second test case, gas entrainment was observed experimentally.

5.3.1 Four intermediate heat exchangers in operation

Bieder et al. (2019) have analyzed and validated the MICAS numerical model for RANS by using a fine meshing of 28 million tetrahedrons. The flow rate was at 90% of nominal power that is 371.8 m^3/h. After having optimized the quality of the meshing for the study presented here, it is necessary to validate again the numerical approach for the new meshing. For this purpose, a different MICAS experiment with lower flow rate is analyzed with RANS. Especially the flow field close to the IHX inlets is addressed here.

The total flow rate of this additional test case was 257.7 m^3/h. The flow was distributed at the core exit according to 95.5 % from the fissile zone, 1.1 % from the reflector zone and 3.4% from the storage zone. Beck et al. (2017) gave more details on these zones. In the current study, all four heat exchangers were in operation. An optimized mesh of 14 million tetrahedrons was built. All tetrahedrons are of similar size and quality. The quality optimization criteria was the minimization of the smallest angles of the tetrahedrons. Initial condition at t = 0 s represents a stagnant velocity field ($\vec{u} = 0$). A stabilized flow field with low temporal velocity fluctuations was achieved after a transient of about 65 s by applying constant boundary conditions.

In the Fig.10, the instantaneous flow field in the MICAS facility is shown for the instant t = 120 s of the transient. The flow in a vertical plane at 0° is visualized. The magnitude of velocity is shown in color scale and the corresponding velocity vectors indicate the directional behavior of flow; vectors are projected on the plane.

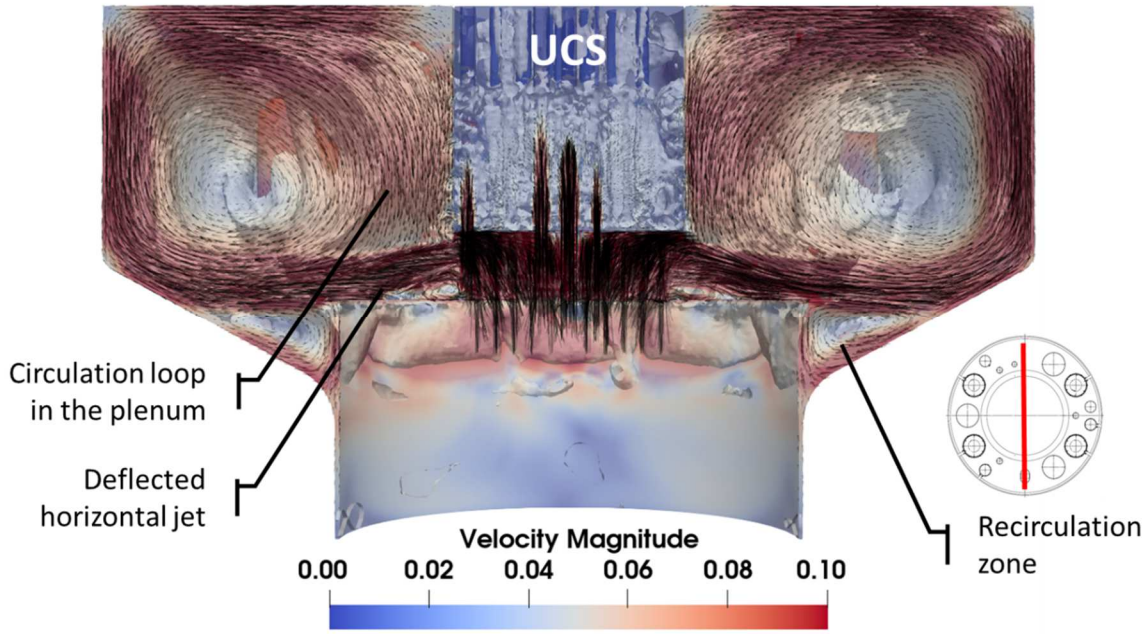

Fig.10 Vertical cut section at the angle 0° of MICAS showing the velocity magnitude in color scale with velocity vectors, which indicate the flow direction

The flow field shows large circulation loops driven by the horizontal jet. In fact, the bottom grid and the ACS deflect the flow in horizontal direction, which initially enters the hot pool vertically. In accordance to the experiment, approximately 5% of the flow enters the ACS. The flow leaves the ACS through the flow holes in the ACS cylindrical outer wall. The momentum of the deflected horizontal jet is strong enough to hit the facility's sidewall, where it then rises towards the free surface. The flow moves farther along the free surface in direction to the ACS where it turns downward to join again the horizontal jet forming in this way an extended circulation loop. A smaller recirculation zone exists between horizontal jet and Redan (wall that separates hot and cold pool, see Fig.10).

In the Fig.11 the flow field in the MICAS facility is shown in a vertical plane at 60°, which passes by the heat exchangers IHX1 and IHX3. The magnitude of velocity is shown in color scale (in m/s) and the corresponding velocity vectors indicate the directional behavior of flow; vectors are projected in the plane. Due to the non-symmetric arrangement of the plenum internals, the flow field is not symmetric.

Between ACS and IHX3, the flow field shows large circulation loops driven by the horizontal jet. The bottom grid and the ACS deflect the flow in horizontal direction. The deflected horizontal jet hits the heat exchanger basis and the facility's sidewall, where it then rises towards the free surface. The flow moves farther along the free surface in direction to the ACS where it turns downward to join on the one hand the horizontal jet forming in this way an extended convection loop. On the other hand, a part of the convection loop enters the heat exchanger directly. A smaller recirculation zone exists between horizontal jet and Redan. The flow traveling in parallel to the free surface does not develop small-scale swirls, which have been detected visually in the experiment.

Between ACS and IHX1, the flow field does not show the large circulation loop. The horizontal jet hits the heat exchanger basis and the facility's sidewall, where it then rises towards the free surface. Then, due to the presence of pump P01, the flow cannot turn and develop radially along the free surface. Thus, the large convection loop cannot develop due to this restriction. Only a small part of the flow passes by the gaps formed between pump P01 and the heat exchangers IHX1 and IHX2, respectively. This flow crossing the gaps creates a small convection loop before being sucked into the heat exchangers. The arrangement of heat exchangers and pumps in the MICAS facility was given in Fig.5 and will be discussed again in Fig.14. Recirculation zones on the free surface were not observed downstream neither of the intermediate heat exchangers nor of pumps and direct heat exchangers.

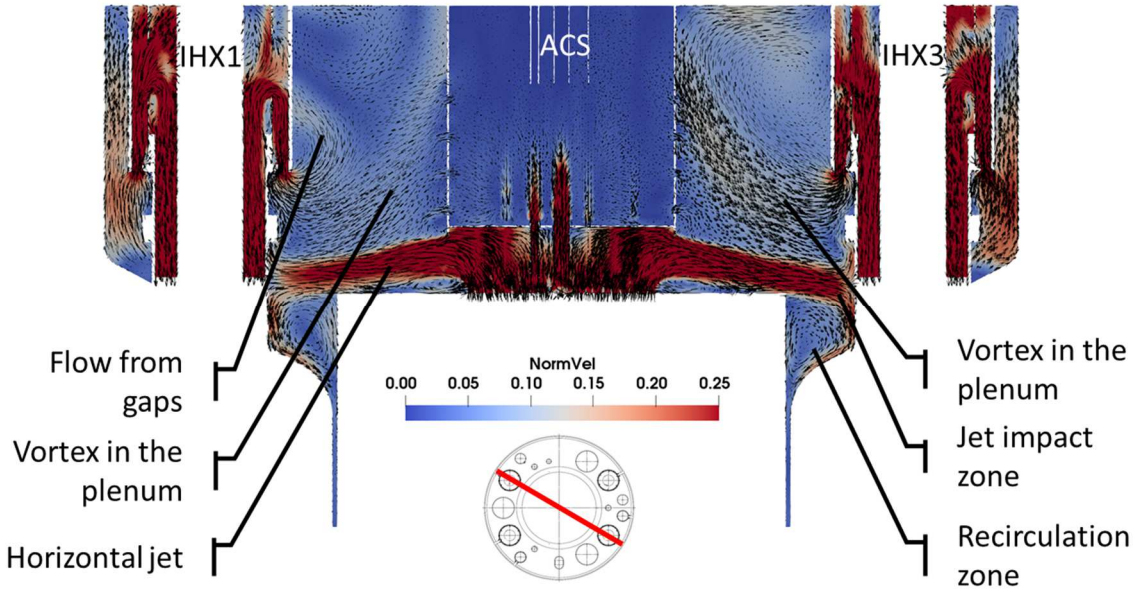

Fig.11 Vertical cut section at the angle 60° of MICAS showing the velocity magnitude in color scale with velocity vectors, which indicate the flow direction

Since the gas-entrainment vortexes are generated at the IHX intakes, the validation of the model is concentrated to this region. Measured and calculated velocity profiles were compared for a measuring plane situated near the heat exchanger IHX2. In fact, Fig.12 shows on the one hand the positions of the measured profiles below the IHX2 intake, H1 and H2 in horizontal direction and V1 and V2 in vertical direction. Due to the LDV measuring method, the experimentally deduces velocity components are aligned to the measuring plane. This plane is positioned between IHX2 and the main coolant pump P01 and is oriented almost normal to the IHX cylindrical wall at an angle of approximately 45°. Location and orientation of this plane is also indicated in Fig.12 by the short red line in the sketch of the facility. On the other hand, measured and calculated horizontal profiles of the horizontal velocity component (H1 an H2) and vertical profiles of the vertical velocity component (V1 and V2) are compared. Taking into account that the circular distribution of the inflow velocity is not homogeneous, the calculated and measured profiles match well. However, the measured vertical velocities close to the IHX intake seem under-predicted. In fact, based on geometrical considerations and known total mass flow, the theoretical vertical velocity at the heat exchanger intake should be about 0.52 m/s what is close to the calculated value. This under-prediction in the experiment might be an effect of the measuring location near the neutrotic shield, which surrounds the heat exchanger intake. The cylindrical neutronic shield around IHX1 and IHX3 is visible in Fig.9. The presence of this shielding inhibits PIV and LDV measurements up to the IHX intake, what might falsify the measurement by leading to too low values. Nevertheless, the overall trend of the calculated velocity profiles followed very well the measurements.

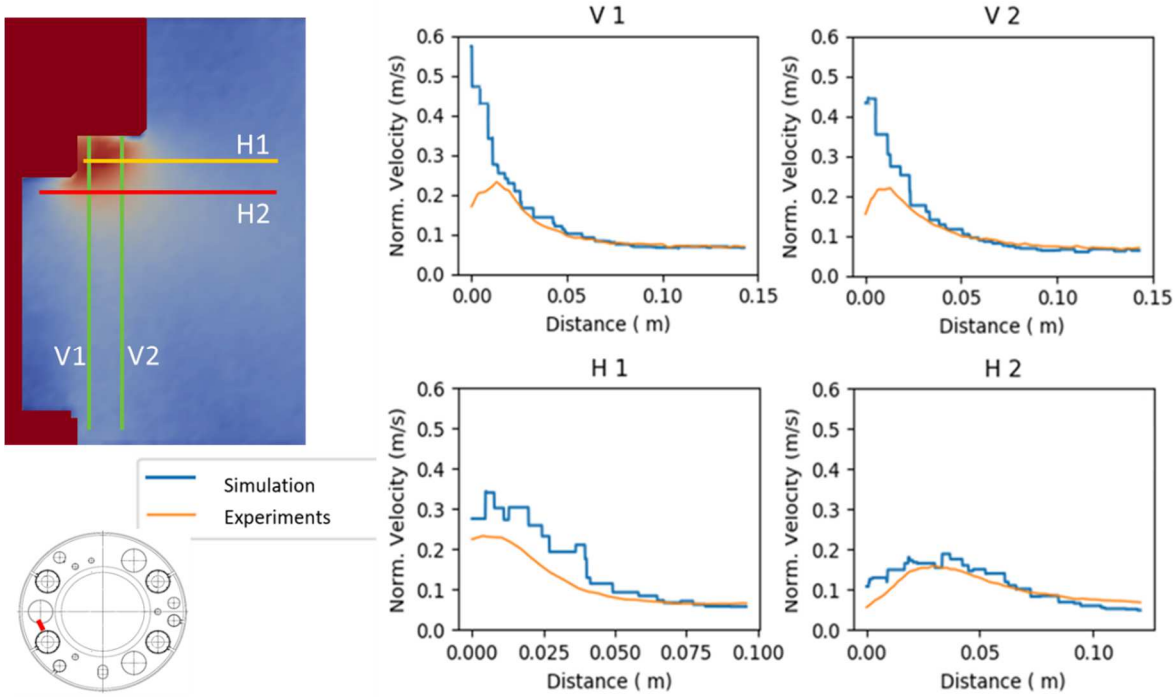

Fig.12 Comparison of measured and calculated velocity profile near IHX2 inlet. V1 and V2 present vertical profiles and H1 and H2 present horizontal profiles

In summary, it can be noted that the RANS calculation can simulate the general behavior of the flow in the upper plenum. Small-scale swills on the free surface were not detected with this calculation, although small swirls were observed experimentally in the wake of the IHXs.

5.3.2 Two out of four intermediate heat exchangers in operation

Various experiments with asymmetric heat exchanger operation have been done in the MICAS facility. In this study, only one experiment with a flow rate at 90% nominal power and two heat exchangers in operation is analysed (IHX3 and IHX4 are closed, see Fig.8 and Fig.9). The total flow rate of water at 22°C is 371.8 m^3/h, which is distributed at the core outlet according to 95.5 % in the fissile zone, 1.1 % in the reflector zone and 3.4% in the storage zone.

a) RANS modelling

The optimized meshing of only 14 million tetrahedrons presented in section 5.3 was used for this study. Initial condition at t = 0 s represents a stagnant velocity field ($\vec{u} = 0$). With the optimized meshing, a quasi-steady state flow field was achieved after a transient of about 45 s by applying constant boundary conditions. Quasi-steady state means here that the main flow field did not vary significantly in time.

In the Fig.13 the flow field in the MICAS facility is shown for the instant t = 60 s of the transient. The magnitude of the flow velocity is visualized in a vertical plane at 60°. The magnitude of velocity is shown in color scale in m/s. The corresponding velocity vectors indicate the directional behavior of flow; vectors are projected in the plane. Between ACS and closed heat exchanger (IHX3), the flow field shows large circulation loops driven by the horizontal jet. The bottom grid and the ACS deflect the flow in horizontal direction, which initially enters vertically the hot pool. The momentum of the deflected horizontal jet is strong enough to hit the heat exchanger basis and the facility's sidewall, where it then rises towards the free surface. The flow moves farther along the free surface in direction to the ACS where it turns downward to join again the horizontal jet forming in this way an extended circulation loop. A small quantity of the flow crosses the closed heat exchanger in a complex path by entering the IHX3 intake at the side directed inward (ACS side) and leaving the heat exchanger at the

side directed outward (facility sidewall side). A smaller recirculation zone exists between horizontal jet and vessel wall.

Between ACS and active heat exchanger (IHX1), the flow does not form a large circulation loop. A zone of low velocity, which represents the center of a large vortex, prevents the formation of the large loop. The bottom grid and the ACS deflect the flow coming from the core in horizontal direction. The momentum of the deflected horizontal jet is strong enough to hit the heat exchanger basis. The horizontal jet is not entering directly into the active heat exchanger. Rather, the jet encircles the heat exchanger bases, rises shortly along the facility sidewall and turns to the side to continue in azimuthal direction in parallel to the facility wall.

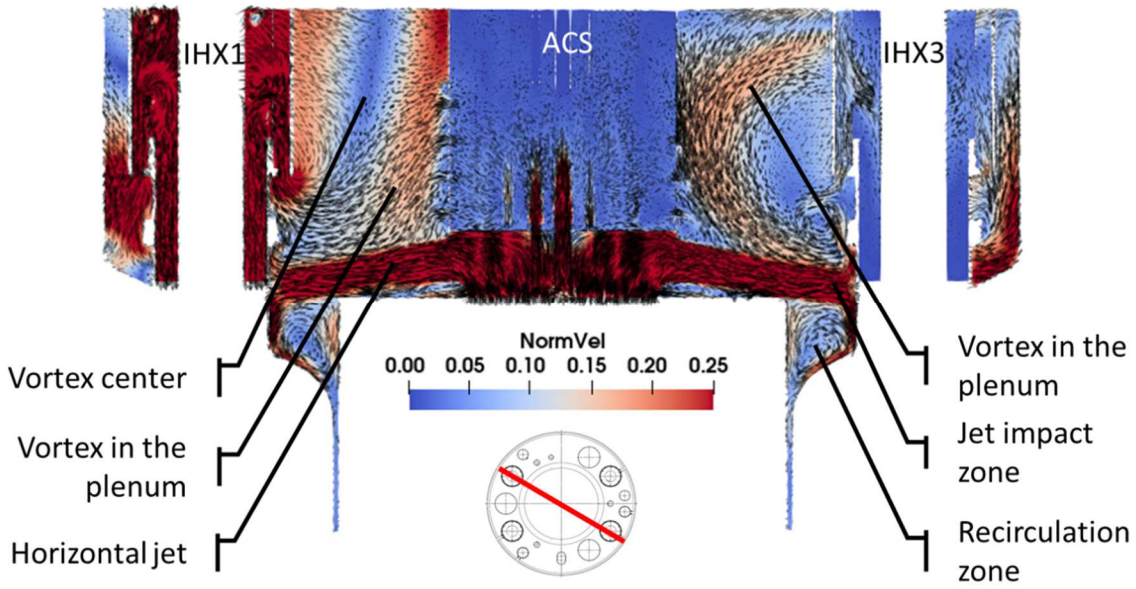

Fig.13 Vertical cut section at the angle 60° of MICAS showing the velocity magnitude (NormVel in m/s) in color scale with velocity vectors, which indicate the flow direction

In the 2D-plot Fig.13, this three-dimensional flow behavior near the active heat exchangers is not well visible. Therefore, in Fig.14 are visualized for the whole calculation domain the flow field by vectors and the pressure distribution in color scale (in Pa). The two counter rotating vortexes near the active IHXs are well visible in both, pressure and velocity. It is also well visible how, on the closed IHXs side, the flow passes between IHX and DHX in order to form the already mentioned large vertical convection loop. On the open IHX side however, the pump represents an obstacle to the flow. The flow that passes between heat exchanges and pump P01 join and accelerate the two counter-rotating vortices. The majority of the flow, however, passes between IHX2 and DHX3 as well as between IHX1 and DHX1.

Fig.15a shows the pressure in a small angular section of 30°. The section encloses in angular direction pomp P01. Its cuts the centers of the swirls that develop between IHX and ACS in their middle. The vortex close to IHX2 is visible as low-pressure tube, which connects the free surface and the IHX inlet. The diameter of the low-pressure tube is about 0.25 m. The size of a vortex related to gas entrainment can be estimated from the photo of Fig.15b. This photo shows the gas core of an entrainment vortex of the analyzed MICAS experiment. The cone on the free surface has a diameter of about 0.03 m and is thus much smaller than the calculated low-pressure tube of Fig.15a. The gas core itself has a diameter of only some millimeters. Besides the incapacity of linear RANS type turbulence models to reproduce correctly swirling flow, the radially small scale of the gas entrainment vortex prevents a numerical representation of the entrainment vortex by using a reasonable fine meshing to model facilities like MICAS.

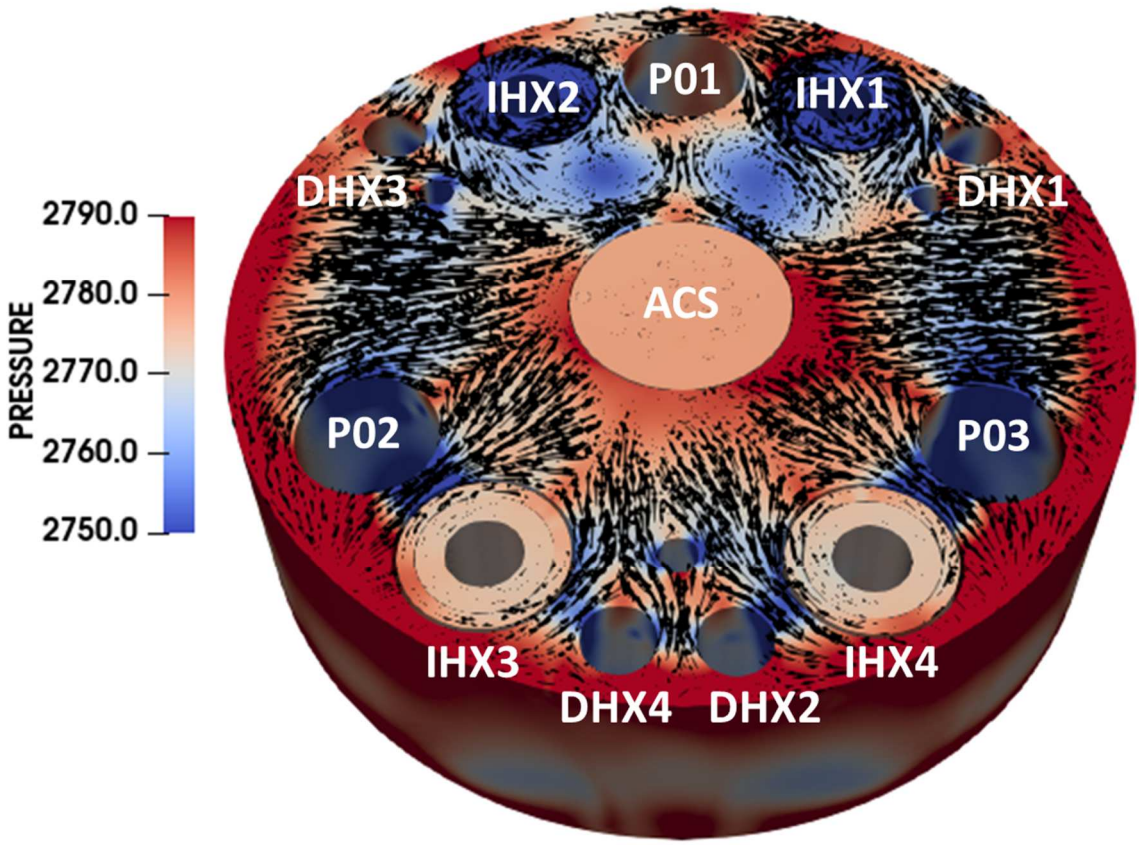

Fig.14 Flow field on the free surface and distribution of the pressure (in Pa) on the limiting surfaces of the calculation domain.

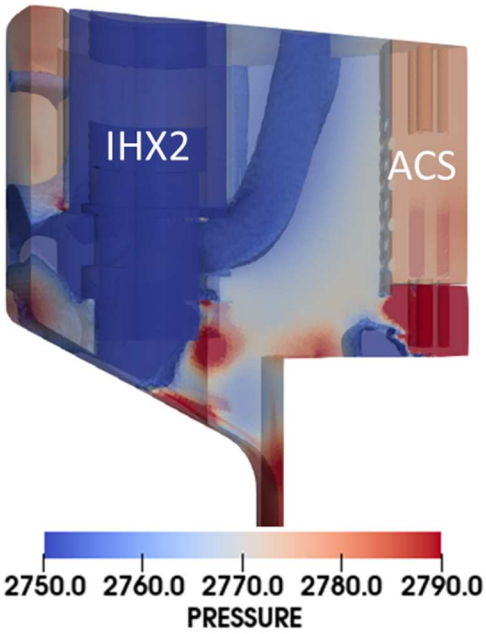

a) Pressure in a sector near IHX2

b) Picture of a gas entrainment vortex

Fig.15 a) Distribution of the pressure (in Pa) close to the IHX with the calculated low-pressure tube of a counter-rotating vortex that connects free surface and IHX2 inlet; b) photo of an entrainment vortex in the MICAS facility

It is evident that the large circulation zones located between the two heat exchangers (IHX1 and IHX2) and the ACS are related to the suction of fluid into the IHX intakes. However, they are radially too extended to represent drain vortexes. Thus, these swirls can mainly be related to the arrangement of the hot pool internals and the increased cross flow velocity due to asymmetric heat exchanger operation. In fact, the swirls are located downwind of the heat exchangers and look like vortexes in the wake of cylinders.

In section 4, we have shown that RANS predict entrainment swirls for the Monji experiment. However, the velocity distribution of the swirls is not correct. Entrainment swirls have not been

observed in the RANS calculation at non-symmetric IHX operation, although they have been observed experimentally. Thus, it seems that it is not possible to estimate gas entrainment with RANS models. Therefore, in accordance to Cristofano and Nobili (2015), the authors have doubts concerning the general applicability of criteria to estimate the risk of gas entrainment that are based on RANS calculations.

b) Large Eddy Simulation

An optimized fine meshing of 52 million tetrahedrons was used for this study. The meshing respects the Taylor scale (eq.(18)) in the open flow zones of MICAS. In three zones the LES was under-resolved: inside the ACS with the guide tubes and the flow holes, in the zone between core outlet and ACS with the bottom plate and significant flow curvature as well as within the IHX, an area without particular interest. Initial condition at t = 0 s represents a stagnant velocity field ($\vec{u} = 0$). With the optimized meshing, a stabilized solution was achieved after a transient of about 45 s by applying constant boundary conditions. Stabilized solution means here that the flow field fluctuates in time around a time invariant mean value.

Fig.16 shows the pressure distribution at 72 s. In order to filter high frequency perturbations, a temporal mean value has been calculated for a period of 0.1 s. On the one hand, the pressure distribution (in Pa) on the free surface is given in this figure. On the other hand, a 3D-contour at 2660 Pa is shown. To better define the location of the displayed detail, the surface meshing of IHX1 and IHX2 are added as well as that of the ACS and the core outlet. The recessed circular surface on the free surface between IHX1 and IHX2 indicates the location of the pump P01, which is not displayed for visual reasons. The ellipse marks two tubes of low pressure called tube A and tube B. These tubes connect the free surface with the heat exchanger intakes. However, the connection is not straight-lined as shown by the gas core in Fig.15b. Rather the low-pressure tube A has a threefold form. Starting from the free surface, the tube descends vertically for about 0.2 m. Then, this tube turns 90° and continues horizontally for about 0.25 m before turning again vertically to reach the inlet of heat exchanger IHX1. The horizontal distance traversed by low-pressure tube B is also about 0.25 m. This tube shows in the horizontal plane a 90° kink before being connected to IHX2. In accordance to the Rankine-vortex discussed in section 3, this tripartite course of the swirl, which has been calculated with the single-phase model, demonstrates the importance of the missing stabilising effect of the gas core on the form of the drain-vortex.

The velocity distribution on the free surface is shown in the vector plot Fig.17, where the vectors are projected into the visualisation plane. The pressure distribution in the plane is added in colour scale. It is well visible that the former discussed low-pressure tubes are located in the centre of a vortex. This is particularly well visible for vortex A. Concerning vortex B, significant cross flow superposes the swirling flow around the low pressure zone so that the circular flow is not easily visible. It has been verified that the vortex structure exists along the whole length of the low-pressure tube from the free surface until the IHX entrances.

During the simulated 30 seconds where the flow is well established, the appearance and disappearance of several low-pressure tubes has been observed in the triangle formed by ACS, IHX1 and IHX2. The associated surface swirls meander slowly around with a lifetime between one and nearly five seconds. The vertical pressure difference at the free surface between vortex centre and vortex outer limit is in the order of 40 Pa. Such a pressure difference will lead on a free surface to a vortex cone of approximately four mm depth when neglecting in the estimation effects of surface tension and circular velocity. Such surface swirls have been observed frequently during the experiment.

It is evident that the calculated swirls and the associated low-pressure tubes with their complex vertical course cannot be related to fully developed gas entrainment vortexes, which show a rather straight vertical course (see Fig.15b). As shown in section 3 for the Rankine-vortex, the gas core stabilises the swirl. Single-phase models cannot simulate this effect. However, the application of two-phase flow models on reactor scale was not possible due to the requested high resolution of the gas core by the meshing. Nevertheless, the calculated swirls might be related to the onset of the formation of a deeper gas core. The presence of such swirls in the calculations with sufficiently well expressed

horizontal pressure differences might be used in the future as indicator for the risk of gas entrainment. This work is under way.

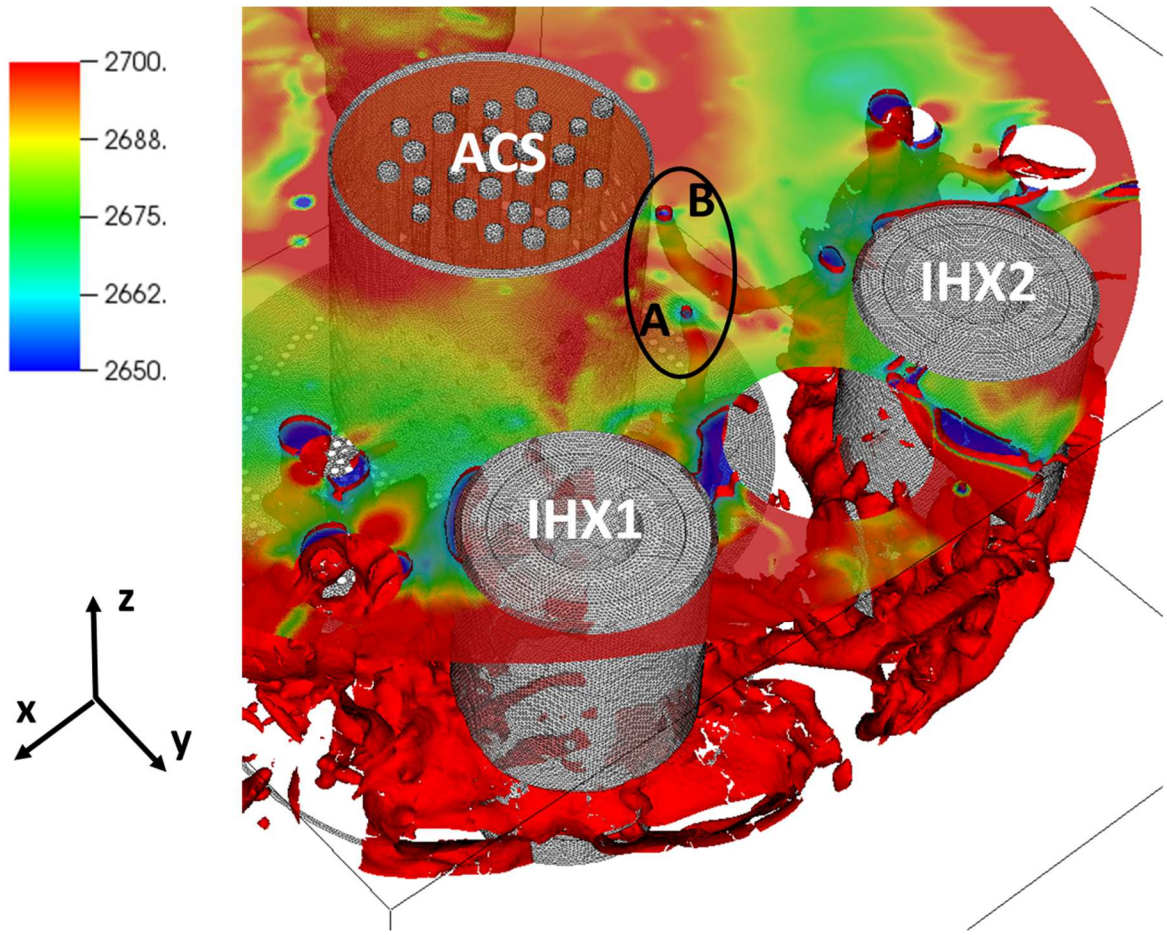

Fig.16 Distribution of the pressure (in Pa) on the free surface at t = 60 s. The 3D-contour at 2650 Pa is added. Temporal mean values of 0.1s are visualized.

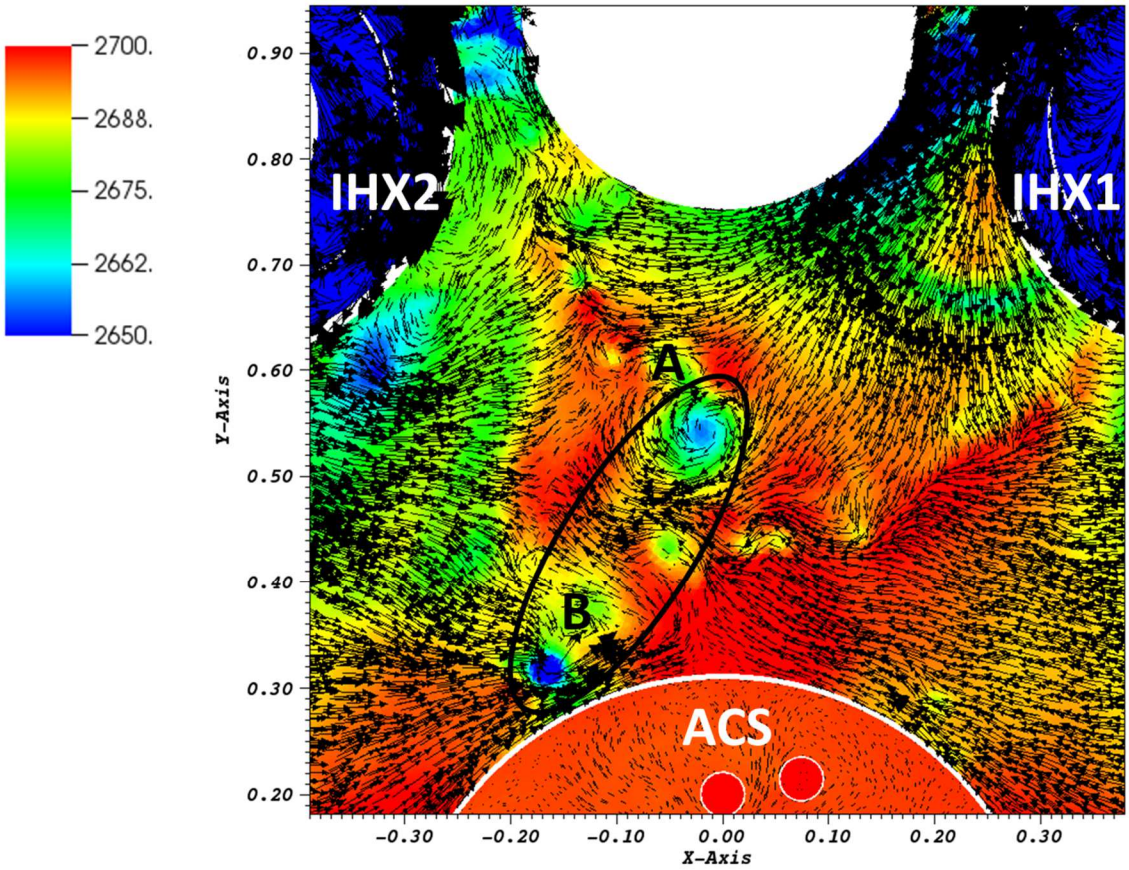

Fig.17 Velocity field, represented by vectors, and pressure field in color scale (in Pa) on the free surface at t = 60 s. Temporal mean values of 0.1s are visualized.

Finally, the temporal mean velocity in the MICAS facility has been calculated over 20 s during the transient between t = 50 s and 70 s. The corresponding vector plot of the distribution of the mean velocity on free surface is shown in Fig.18. The walls of the IHXs are marked in Fig.18 for a better visualization. Two large counter rotating swirls are present in the area between the pump P01, IHX1, IHX2 and the ACS. These swirls cannot been related to the former discussed local vortexes, which are related to the formation of local tube-like zones of low pressure. These large swirls are related to the large recirculation zones that have been predicted with the RANS model as shown in Fig.14. In fact, statistics based RANS approaches predict as per definition temporal averaged flow fields although this modelling approach is used more and more for unsteady flow.

Neither the large swirls nor the flows in the heat exchangers are symmetrically arranged. This flow behavior was calculated in accordance by both turbulence modelling approaches, RANS (Fig.14) and LES (Fig.18). A possible reason for the asymmetry in the LES flow field is a too short time to collect statistics (20 s). Even so, the asymmetric arrangement of some internals in the hot pool of SFRs also leads to an asymmetry in the flow field. As shown recently by Bhatia et al. (2020), especially the arrangement of guide tubes leads to an important dependency of the velocity of the horizontal jet on the azimuthal angle.

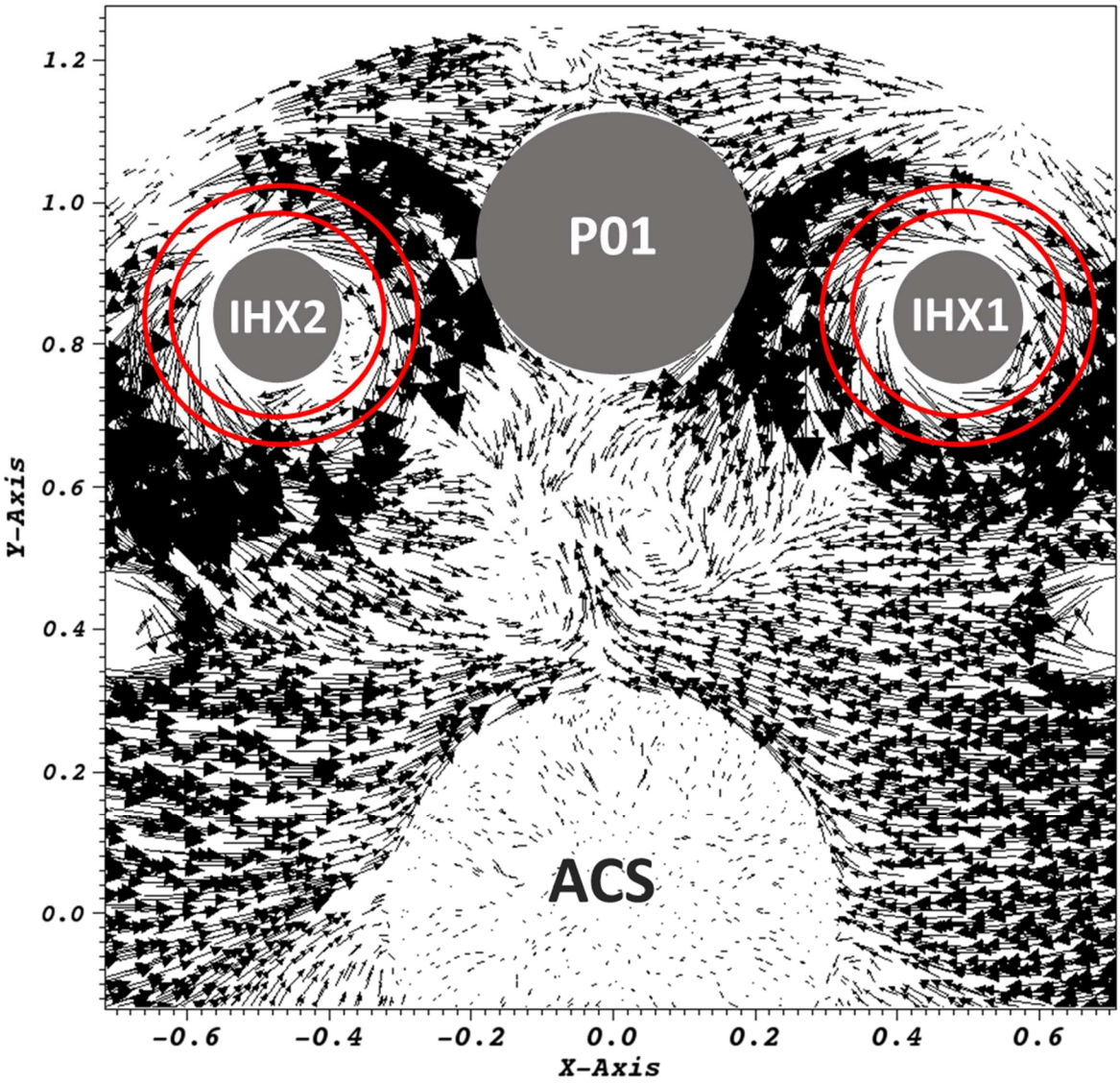

Fig.18 Vector field of the temporal mean velocity on the free surface

6 Conclusion

In compact SFR designs, gas entrainment into the reactor core might happen due to gas-drain vortexes that can be created by the intermediate heat exchangers. Safety authorities request to estimate the risk of such gas entrainment. Thus, a fundamental study has been launched at CEA to assess the possibility of CFD models to predict gas entrainment. This study is based on the Rankine-vortex model, a separate effect study in laboratory size and the results of the integral effect MICAS experimental program, where the formation of surface swirls and gas-drain vortexes were observed for accidental flow conditions. MICAS is a 1/6th scale model of the upper plenum of the 4th generation prototype reactor ASTRID that was developed at CEA. In this facility, two high-quality velocity measurements were realized for CFD validation by applying flow rates at a nominal pump power and for accidental conditions.

- Based on the Rankine-vortex model it is shown that drain vortexes with gas core cannot be calculated correctly by single-phase CFD as the pressure close to the vortex center is a function of the gas core density.
- The assessment of CFD to simulate swirling flow is done on the example of the separate effect experiment of Monji (2004). The analysis of a swirl without deformation of the liquid surface stressed the already well-known fact that turbulence models based on linear RANS could not

calculate correctly the radial distribution of the circular velocity of the vortex. In fact, the maximum circular velocity is underestimated and is located too far from the center of the swirl. With laminar flow hypothesis and LES, the swirl is calculated in accordance to the experiment. This single effect analysis further underlined the difficulties of using tetrahedral cells in combination with collocated arrangement of unknowns to calculate swirling flow.

The assessment of CFD to simulate the flow in a SFR hot pool including gas entrainment is done on the example of the integral effect experiment MICAS. The flow in the hot pool of a SFR is analyzed for two operation conditions of the intermediate heat exchangers (IHXs): all four IHXs in operation and two out of four IHXs in operation. The first case is used as a reference case and for model validation, in particular for the flow near the heat exchanger's intake. In the second case, gas entrainment was observed experimentally.

- For the case of all four heat exchangers in operation, large, vertically arranged convection loops establish in the facility. Recirculation zones on the free surface, downstream of the heat exchangers, were not observed. The overall flow field in the facility as well as the velocity profiles, which were measured at an IHX intake, are well reproduced by the RANS calculation.
- For the case of two out of four heat exchangers in operation, large, vertically arranged convection loops establish in the hot pool.
  - Extended recirculation zones with counter rotating vortexes were observed in the RANS calculation on the free surface. These recirculation zones, which connect vertically from the free surface to the IHX intakes, are located in the wake of the heat exchangers in operation. Thus, the swirls are related to the arrangement of the IHXs in the hot pool and the non-symmetric flow field. Small gas-drain swirls were not observed in RANS calculations. The authors have doubts on the applicability of criteria to estimate the risk of gas entrainment, which are based on RANS calculations.
  - In the temporally averaged LES flow field, extended recirculation zones were predicted in the wake of the IHXs. These vortexes are in accordance to the RANS calculation. Additionally, small drain-type vortexes were calculated by LES downstream of the active heat exchangers in the area between IHXs and Above Core Structure. The swirls develop in the instantaneous flow field and meander around in time. The vortexes connect in a non-regularly descending swirling tube the free surface and the IHX intakes. As shown for the Rankine-vortex, if gas entrainment happens, the gas core will stabilize the form of the drain-vortex. Single-phase models, however, cannot take into account this stabilizing gas core. Thus, the observed vortexes can be related only to the onset of the formation of a drain vortex. Nevertheless, their presence in the LES can indicate a certain risk of gas entrainment.

For advanced gas-entrainment modelling, it is planned to use the front-tracking model of TrioCFD to simulate the free surface. Concerning the analysis of further MICAS experiments, it is intended to analyses experiments with significant thermal effects.

Acknowledgement

This work was granted access to the HPC resources of CINES and IDRIS under the allocation A0092A07571 made by GENCI.

References

P.-E. Angeli, U. Bieder U., G. Fauchet, 2015 Overview of the Trio_U code: Main features, V&V procedures and typical applications to engineering, 16th International Topical Meeting on Nuclear Reactor Thermal Hydraulics, NURETH-16, Chicago, USA (2015)

P.-E. Angeli, M.-A. Puscas, G. Fauchet and A. Cartalade: FVCA8 Benchmark for the Stokes and Navier–Stokes Equations with the TrioCFD Code—Benchmark Session. In: Finite Volumes for Complex Applications VIII - Methods and Theoretical Aspects, pp.181-202 (2018)

T. Beck, V. Blanc, J.M. Escleine, D. Haubensack, M. Pelletier, M. Phelip, B. Perrin and C. Venard (2017) Conceptual design of ASTRID fuel sub-assemblies. Nucl. Eng. and Design 315, 51–60 (2017)

H. Bhatia, U. Bieder, Y. Gorsse and D. Guenadou (2020) Thermal-hydraulic analysis of the flow in the MICAS experimental facility using CFD. Computational fluid dynamics for nuclear reactor safety conference (CFD4NRS-8), 25-27 November 2020, Paris, France

Bieder U. (2012) Analysis of the flow down- and upwind of split type mixing vanes. Computational fluid dynamics for nuclear reactor safety conference (CFD4NRS-4) 10-12 September 2012, Daejeon, Corée de Sud

U. Bieder, G. Ziskind, A. Rashkovan (2018) CFD analysis and experimental validation of steady state mixed convection sodium flow". Nucl. Eng. and Design, 326 (2018) 333-343

U. Bieder, J. Maillard, Y. Gorsse, D. Guenadou (2019) CFD analysis of the flow in the MICAS experimental facility, a water model of the hot pool of a sodium cooled fast reactor. Nucl. Eng. and Design, 350 (2019) 67-77

L. Cristofano, M. Nobili (2015) Influence of boundary conditions in numerical simulation of free surface vortices. Energy Procedia 82, 2015, 893 – 899 Numerical evaluation of gas core length in free surface vortices

L Cristofano, M Nobili and G Caruso (2014) Numerical evaluation of gas core length in free surface vortices. Journal of Physics: Conference Series 547 (2014) 012030

Crouzeix M., Raviart P.-A., Conforming and nonconforming finite element methods for solving the stationary Stokes equations, R.A.I.R.O. Anal. Num´er. 7 R3 (1973), 33–76.

J. H. Ferziger and M. Peric (2002) Computational Methods for Fluid Dynamics. Springer Verlag BerlinD. Grand, R. Vidil, D Taillifet, J.-P Benque Problèmes posés par la convection mixte du sodium dans les réacteurs rapides : Modélisations physique et numérique. In French. La Houille Blanche, N° 2/3, 1979

D. Guenadou, I. Tkatshenko and P. Aubert (2015) Plateau Facility in Support to Astrid and the SFR Program: An Overview of the First Mock-Up of the Astrid Upper Plenum, MICAS. *Proceedings of the16th International Topical Meeting on Nuclear Reactor Thermal Hydraulics (NURTEH16)*, Chicago, Illinois, August 30-September 4 (2015).

D. Guenadou, P. Aubert, V. Biscay, M. Bottin, J-P. Descamps (2016) Study of the Free Surface Flow in the MICAS Mock-Up in Support of the ASTRID SFR Program. *Proceedings of the 11th International Topical Meeting on Nuclear Reactor Thermal Hydraulics, Operation and Safety (NUTHOS-11)*, Gyeongju, Korea, October 9-13 (2016).

D. Guenadou, P. Aubert, V. Biscay and J-P. Descamps (2017) Flow analysis in the upper plenum of the MICAS model in support of the ASTRID reactor program. *Proceedings of the16th International Topical Meeting on Nuclear Reactor Thermal Hydraulics (NURTEH17)*, Xi'an, China, September 3-8 (2017)

T. Höhne, S. Kliem and U. Bieder (2018) IAEA CRP benchmark of ROCOM PTS test case for the use of CFD in reactor design using the CFD-Codes ANSYS CFX and TrioCFD Nucl. Eng. Des., 333 (2018) 161-180

H. Hoffmann (1989) Thermohydraulic investigations of decay heat removal systems by natural convection for liquid–metal fast breeder reactors. Nuclear Technology (1989) 88 (1), 75–86

H. Hoffmann, K. Hain, K. Marten, H. Ohira, K. Rust, D. Weinberg (1994) The status of thermal hydraulic studies on the decay heat removal by natural convection using RAMONA and NEPTUNE model. Proceedings of the 4th International Topical Meeting on Nuclear Reactor Thermal Hydraulics (NURTEH4), Taipei, Taiwan, April 6-9 (1994)

I. Idel'cik (1969). Mémento des pertes de charges singulières et de pertes de charges par frottement [Handbook of singular and friction head losses]. Eyrolles, Paris

A. Issa (2010) Etudes hydrauliques de l'influence des géométries des bassins sur l'alimentation des pompes. PhD thesis in French at the École Nationale Supérieure d'Arts et Métiers, ParisTech, 2010

K. Ito, H. Ohshima, T. Sakai and T. Kunugi (2010) CFD-based Evaluation of Interfacial Flows. In: Computational Fluid Dynamics, Book edited by: Hyoung Woo OH, pp. 420, January 2010, INTECH, Croatia

Kimura N. Ezure T., Tobita A. and Kamide, H (2008). Experimental study on gas entrainment at free surface in reactor vessel of a compact sodium-cooled fast reactor, Journal of Nuclear Science and Technology, Vol. 45, 1053-1062.

Lefevre, J.C., et al., 1996. European fast reactor design. Nucl. Eng. Des. 162 (2–3),133–143.

W. Marth (1993) The Story of the European Fast Reactor Cooperation. KfK-Bericht, KfK 5255, Dezember-1993

E. Merzari, H. Ninikata, S. Wang and E. Baglietto (2009) Numerical simulations of free-surface vortices Nuclear technology 165, 2009

H. Monji, Akimoto, T., Miwa, D., and Kamide, H. (2004) Unsteady Behavior of Gas Entraining Vortex on Free Surface in Cylindrical Vessel, Proc. 4th Japan-Korea Symposium on Nuclear Thermal Hydraulics and Safety, Sapporo, pp. 190–194, 2004.

H. Monji, T. Shinozaki, H. Kamide, T. Sakai (2010) Effect of Experimental Conditions on Gas Core Length and Downward Velocity of Free Surface Vortex in Cylindrical Vessel. Journal of Engineering for Gas Turbines and Power, 2010, Vol. 132 / 012901-1

S. Moriya (1998). Estimation of hydraulic characteristics of free surface vortices on the basis of extension vortex theory and fine model test measurements, CRIEPI Abiko Research Laboratory Report, No. U97072 (in Japanese).

B. Moudjed, J. Excoffon, R. Riva, L. Rossi (2016) Experimental study of gas entrainment from surface swirl. Nuclear Engineering and Design xxx (2016) xxx–xxx

S. Mulligan, G. De Cesare, J. Casserly and R. Sherlock (2018) Understanding turbulent free surface vortex flows using a Taylor-Couette flow analogy. Sci Rep 8, 824.

F. Nicoud, F. Ducros: "Subgrid-scale stress modelling based on the square of the velocity gradient tensor". Flow Turb. Comb., 62, pp. 183-200 (1999)

I.S. Park and C.H. Sohn (2011) Experimental and numerical study on air cores for cylindrical tank draining. Int. Comm. in Heat and Mass transfer 38, 2011, 10441049

S. B. Pope (2000): "Turbulent Flows", Cambridge University Press, Cambridge, 2000.

H. Reichardt, 1951. Vollständige Darstelling der turbulenten Geschwindigkeitsverteilung in glatten Leitungen. Zeitschrift für Angewandte Mathematik und Mechanik, Vol 31, p 208

W.A. Rankine (1858) A Manual of Applied Mechanics. 9th Ed., C. Griffin and Co., London, UK.

S.B. Rodriguez, F. Espinoza, S.L. Steinberg and M.S. El-Genk (2012) Towards a Unified Swirl Vortex Model. Sandia National Laboratories, SAND2012-0840C

G. Rodriguez, J.-F. Dirat, A. Traina and M. Christofari (2015) Qualification program of the ASTRID SFR project: Definition, Methodology and associated Risk Evaluation & Management. Proceedings of ICAPP conference, May 03-06, 2015, Nice, France, Paper 15093

T. Sakai, Y. Eguchi, H. Monji, K. Ito and H. Ohshima (2008) Proposal of Design Criteria for Gas Entrainment from Vortex Dimples Based on a Computational Fluid Dynamics Method, Heat Transfer Engineering, 29:8, 731-739

K. Satpathy (2012) Studies on Prediction of Gas Entrainment Inception in Hot Pool of Liquid Metal Fast Reactors. PhD thesis Enrolment number: PHYS02200704003 Indira Gandhi Center for Atomic Research, Kalpakkam, India

A Škerlavaj, A Lipej, J Ravnik and L Škerget (2010) Turbulence model comparison for a surface vortex simulation. IOP Conf. Series: Earth and Environmental Science 12, 2010, 012034

D. Tenchine (2010) Some thermalhydraulic challenges in Sodium cooled fast reactors, Nuclear Engineering and Design (2010), 240, 1195–1217

D. Tenchine, C. Fournier and Y. Dolias (2014) Gas entrainment issues in sodium cooled fast reactors. Nuclear Engineering and Design 270 (2014) 302–311

D. Weinberg, K. Rust, H. Hoffmann, 1996 Overview report of RAMONA-NEPTUN Program on passive decay heat removal, Forschungszentrum Karlsruhe, Report FZKA 5667, 1996

ANALYSIS OF THE FLOW IN THE HOT POOL OF SODIUM COOLED FAST REACTORS WITH RESPECT TO THE RISK OF GAS ENTRAINMENT

H. Bhatia[1], U. Bieder[1] and D. Guenadou[2]

[1]DES-STMF, CEA, Université Paris-Saclay F-91191 Gif-sur-Yvette, France
[2]CEA Cadarache, DTN/STCP/LHC, F-13108 Saint Paul lez Durance, France

The flow in the hot pool of a compact SFR is investigated in the MICAS facility. Computational Fluid Dynamics is used to assist the interpretation of experiments by multi-scale calculations. Special attention is given to the risk of gas entrainment into the reactor core due to the formation of drain-type vortexes at the intermediate heat exchanger intakes (Fig.1 left figure).

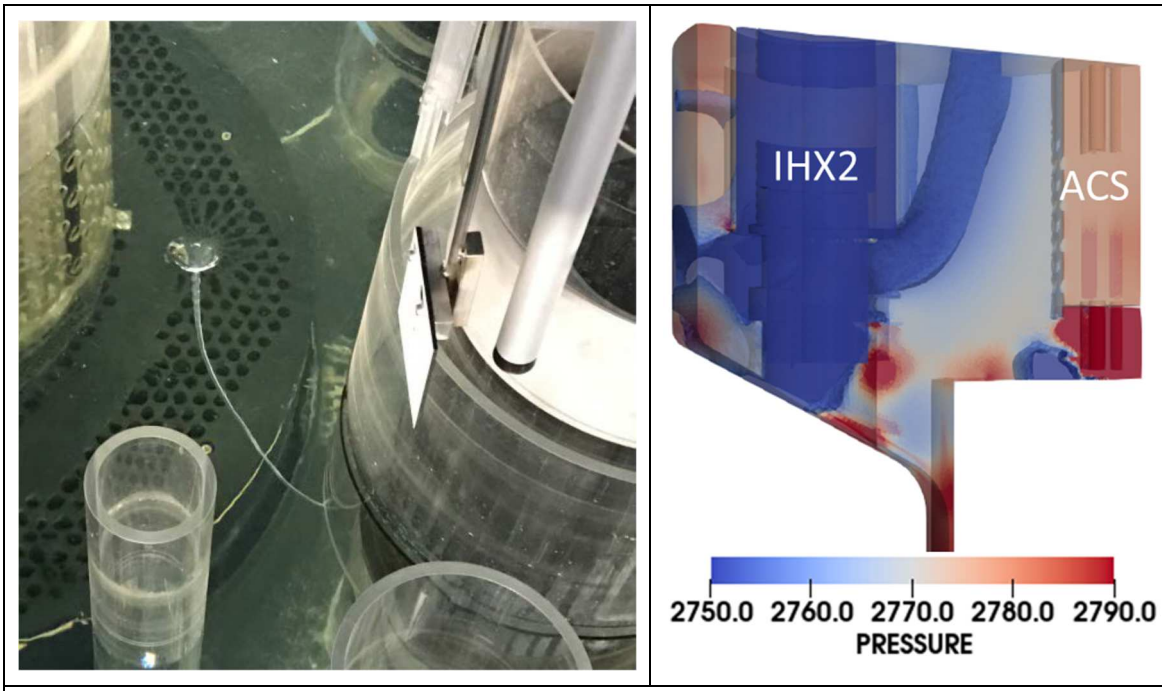

Fig.1 Photo of an entrainment vortex in the MICAS facility (left side) and distribution of the pressure (in Pa) close to the intermediate heat exchanger (right side)

The fact that linear RANS models cannot simulate correctly swirling flow was confirmed by single effect studies. The size of the calculated vortex is overestimated as visible in the pressure distribution close to the heat exchanger on the right hand side of Fig.1. LES is able to simulate the onset of gas entrainment; however, the missing gas core in single-phase calculations inhibits a correct prediction of well-established drain vortexes.